

DELFT UNIVERSITY OF TECHNOLOGY

APPLIED PHYSICS MASTER THESIS  
AP3902PMT

---

The effect of intermediate band trap  
centres on the charge-carrier dynamics in  
all-inorganic mixed-halide perovskite  
thin films.

---

*Author*

Menke Knol (5185130)

*Supervisors*

Dr. Ir. Tom J. Savenije (TU Delft)  
Prof. Dr. Bruno Ehrler (AMOLF)

*Daily Supervisors*

Jiashang Zhao (TU Delft)  
Moritz Schmidt (AMOLF)

*External Assessment Committee Member*

Dr. Stephan W.H. Eijt (TU Delft)

December 3, 2021

# The effect of intermediate band trap centres on the charge carrier-dynamics in all-inorganic mixed-halide perovskite thin films.

## Abstract

Photovoltaics will play an essential part in the inevitable energy transition at hand that is needed for a sustainable future fueled by renewable energy sources. As one of the most promising emerging types of photovoltaic materials, perovskite solar cells (PSCs) can contribute to this transition, but intrinsic stability issues limit the widespread application. By introducing all-inorganic mixed-halide perovskites (MHPs), the thermal stability is addressed, but the power conversion efficiency (PCE) needs to improve. The goal of this thesis is to investigate the temperature-dependence of the charge-carrier dynamics in all-inorganic CsPbI<sub>2</sub>Br thin films, which includes the quantification of non-radiative recombination losses through electronic defects in the material. By using both the time-resolved microwave conductivity (TRMC) measurement method and deep-level transient spectroscopy (DLTS), the aim is to provide a unified kinetic model that describes the recombination dynamics of free charges inside the perovskite layer. By fitting the TRMC measurements, physical parameters such as the electronic mobilities and the governing rates of the intermediate band trap centres can be extracted. Using DLTS, the emission rates from electronic defects can be extracted and the corresponding activation energies can be compared with the values obtained using TRMC. The analysis of these results shows that the activation energies for the emission processes of both methods are inconsistent and this mismatch can be due to either measurement method. The TRMC measurements were fitted using too restrictive fitting parameter boundaries, but first attempts at using a wider boundary range show that constraining the temperature-dependence of the parameters using a physical approach is needed to fit the measured traces. The DLTS measurements were performed for different filling pulse lengths and these suggest similar processes being at play despite the lowering of the activation energies for longer filling pulses, which indicates that at least one of the two processes has an ionic nature. By increasing the temperature resolution of the DLTS measurements, the uncertainty in the determination of the activation energies can be reduced and stronger conclusions can be drawn on the physical origin of the capacitance transients and how to compare these to the TRMC measurements. In addition to decreasing the temperature step size, increasing the range of illumination intensities and lengthening the measurement times are proposed to improve the quality of the TRMC fits. However, uncertainties remain in the assumptions made for the kinetic model that is applied to fit the TRMC data and further research is needed to obtain a clear picture of the charge-carrier dynamics in all-inorganic mixed-halide perovskite thin films.

# Contents

<b>1</b>	<b>Introduction</b>	<b>3</b>
<b>2</b>	<b>Theory</b>	<b>5</b>
2.1	Perovskite materials . . . . .	5
2.2	Perovskite solar cells . . . . .	7
2.3	Charge-carrier and recombination dynamics . . . . .	9
2.3.1	Temperature-dependent charge-carrier dynamics . . . . .	10
2.4	Time-Resolved Microwave Conductivity . . . . .	13
2.5	Deep-Level Transient Spectroscopy . . . . .	17
2.6	Research question . . . . .	20
<b>3</b>	<b>Methodology</b>	<b>21</b>
3.1	Sample Preparation . . . . .	21
3.1.1	Perovskite Thin Film Preparation . . . . .	21
3.1.2	Device Fabrication . . . . .	21
3.2	Characterisation . . . . .	21
3.2.1	Structural Characterisation . . . . .	21
3.2.2	Optical Characterisation . . . . .	21
3.2.3	Device Characterisation . . . . .	21
3.3	TRMC . . . . .	22
3.4	DLTS . . . . .	22
<b>4</b>	<b>Results</b>	<b>23</b>
4.1	Characterisation . . . . .	23
4.1.1	Structural Characterisation . . . . .	23
4.1.2	Optical Characterisation . . . . .	23
4.1.3	Device Characterisation . . . . .	25
4.2	TRMC . . . . .	27
4.3	DLTS . . . . .	35
4.3.1	Fitting parameters . . . . .	36
<b>5</b>	<b>Discussion</b>	<b>40</b>
<b>6</b>	<b>Outlook</b>	<b>42</b>
<b>7</b>	<b>Conclusion</b>	<b>46</b>
<b>8</b>	<b>Acknowledgements</b>	<b>47</b>
<b>9</b>	<b>Appendix</b>	<b>52</b>

# 1 Introduction

Since the industrial revolution, human action has warmed the earth by more than 1.2 degrees Celsius and without any further measures, this rise will continue during the coming decades [1]. The recently published Sixth Assessment Report by the IPCC provides unequivocal evidence for this development and gives a final warning that major cuts in the carbon emissions are required to stay below the 1.5 degrees warming as discussed in the 2015 Paris Agreement [2, 3]. An essential part of working towards a sustainable future is stepping away from fossil fuels and moving towards renewable energy sources [2]. In 2020 renewable energy sources provided 29% of the global electricity demand, and this year this figure is believed to increase by another 8% [4]. Solar energy currently plays a modest role in the energy transition, providing only a few per cent to global energy, but it has enormous potential due to the sheer magnitude of the total solar radiation that hits the earth's surface [4, 5]. To put things into perspective, the amount of energy provided by the total solar radiation is four orders of magnitude larger than the global energy consumption [6].

## Photovoltaics

Photovoltaics are the most common type of solar power, a field in which more than 90% of the energy comes from industry-standard crystalline silicon (c-Si) based solar panels [7]. The performance warranty of a c-Si-based module exceeding 20 years and a record PCE for a c-Si-based device of 26.7%, explain the widespread commercial application of the c-Si absorber layer [8, 9]. The main downfall is that c-Si requires an energy-consuming production method in a strictly controlled environment since a high purity of the crystal structure is required, due to the low defect tolerance of the material [10]. Since c-Si is an indirect-bandgap absorber layer, the absorption coefficient of the material is relatively low and a thick layer is needed to absorb a sufficient amount of light [10, 11]. Thus, research is done towards next-generation solar cells and one of the most promising types of materials in this field is the metal halide perovskite (MHP) semiconductor.

## Perovskite solar cells

This thin-film solar cell has seen a tremendous increase in its power conversion efficiency (PCE) over the past decade, from a record PCE of 3.8% in 2009 towards its current 25.8% record for a single-junction device [12, 13, 14]. Along with this fast rise in PCE, perovskite solar cells (PSCs) only require a thin absorber layer due to their high absorption coefficient [15]. Additionally, the bandgap-tunability makes PSCs suitable for tandem-cell applications, the PCE of which already has achieved 29.5% [16, 14, 17]. Lastly, the production process of PSCs is potentially low-cost as it is based on low-temperature solution-based processing [18]. However, there are still some bottlenecks that limit the commercialisation of PSCs. For the most common organic-inorganic perovskites, the material is thermally unstable at temperatures that fall within the standard operating conditions in real-life photovoltaic applications [19]. The proposed solution is an all-inorganic perovskite layer, but up until now, the PCE has been lacking behind the record-holding PSC, with a current record of 16.1% [20].

## Research topic

This thesis focuses on the charge-carrier dynamics in these all-inorganic perovskites to get better insight into how charges behave and are affected by defects in the material after being generated. The aim is to provide a better understanding that will lead to an improvement of the material development and an increase in the photovoltaic performance. In Section 2.1 the material structure will be explained, followed by an elaboration on the PSC device with the all-inorganic mixed-halide PVK layer as photoactive layer in Section 2.2. Afterwards, in Section 2.3.1 the physics behind the charge-carrier dynamics inside the material will be explained and the two methods that will be used to investigate them, namely time-resolved microwave conductivity (TRMC) in Section 2.4 and deep-level transient spectroscopy (DLTS) in Section 2.5. The end goal of this thesis is to provide a unified

kinetic model that describes the temperature-dependent charge-carrier dynamics of the all-inorganic mixed-halide perovskite thin films, including the quantification of trap-assisted non-radiative recombination losses through defects in the material. After explaining both measurement methods, in Section 2.6 the exact means of answering this research question will be elaborated on further.

## 2 Theory

### 2.1 Perovskite materials

The group of compounds called perovskites are crystals that share the same perovskite formula  $ABX_3$ , where A is a monovalent cation, B is a divalent cation and the X positions are occupied by monovalent anions, as shown in Figure 3.

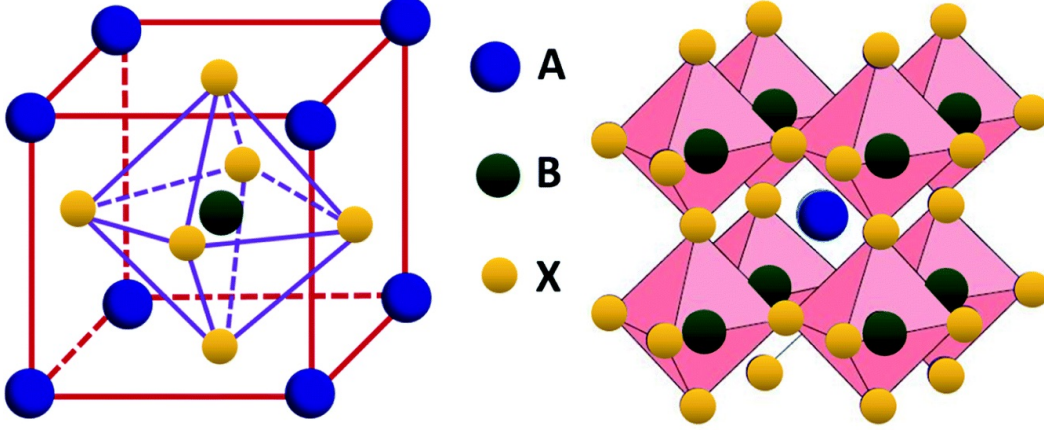


Figure 3: The perovskite structure, consisting of connected octahedra and a cation filling up the gaps. Reproduced from ref. [21].

The divalent cations form corner-sharing octahedra with the anions and the monovalent cations, which are in general larger atoms than the B cations, fill up the space inside the octahedra. The most studied configurations of perovskite in the field of photovoltaics contain either the organic methylammonium ( $MA^+$ ), formamidinium ( $FA^+$ ) or the inorganic caesium ( $Cs^+$ ) as the monovalent cation [22]. Lead ( $Pb^{2+}$ ) has proven to be the best-performing divalent cation, while the halides iodide ( $I^-$ ), bromide ( $Br^-$ ) or chloride ( $Cl^-$ ) are the most common anions [23]. In the most-studied configuration  $MAPb(I_xBr_{1-x})_3$ , it was found that mixing the halides allowed for bandgap tuning of the photoactive perovskite. The halide electronic orbitals strongly determine the level of the valence band maximum (VBM), and by for example adding bromide to the full-iodide configuration, the bandgap increases [24]. This feature makes it possible to finetune the photoactive material for different purposes, such as the top layer of a tandem solar cell.

#### All-inorganic as solution

Despite these useful features, there are difficulties that limit the widespread use of PSCs. One major limitation is the thermal instability in the higher regions of standard solar cell operating temperatures of PSCs with organic cations, especially with the highly volatile  $MA^+$  [19]. One can solve this issue by replacing  $MA^+$  with the inorganic cation caesium, forming an all-inorganic MHP, which has shown to be more resilient to stresses caused by the illumination of the material [25]. Initially, it was assumed that the organic  $MA^+$  made a significant contribution to the charge carrier mobility and subsequently cause the high PCE [26]. Since the achieved mobilities for all-inorganic materials are of the same order, it is now thought to have its origin in the inorganic part of the structure, paving the way for the replacement of  $MA^+$  by  $Cs^+$  [25]. One of the commonly-studied all-inorganic perovskites,  $CsPbI_3$ , has a bandgap of  $E_g = 1.73$  eV in its cubic  $\alpha$ -phase, which is suitable for photovoltaic applications [27]. However, the problem with this material is that this cubic phase forms at high temperatures exceeding 300 K and it easily degrades to the orthorhombic non-perovskite  $\delta$ -phase [27, 28]. Mixing the halides improves this insufficient phase stability at room temperature (RT), by partially replacing iodide with bromide. The resulting all-inorganic mixed-halide  $CsPbI_2Br$  has increased stability of the cubic  $\alpha$ -phase, due to the increased Goldschmidt's tolerance factor and with its bandgap of around  $E_g = 1.9$  eV, it is suited for tandem solar cell applications [29, 27]. Just as for the single-halide material, it is energetically favourable for  $CsPbI_2Br$  to crystallise into the orthorhombic  $\delta$ -phase at RT.

However, by annealing the transition can be made to the cubic phase followed by 'freezing' the crystal phase by rapidly cooling the material down to RT. The phase transition from non-perovskite to cubic perovskite phase can be observed by the eye since the colour of the material changes from a bright yellow to black [25].

### Remaining challenges

Even with the improved phase stability, two main issues remain in this class of material properties, namely the instability under ambient conditions and the light-induced phase segregation. The first problem implies that exposure to oxygen and moisture causes the material to decay to the non-perovskite phase [30]. The most straightforward method of solving this issue is by encapsulating the material, but other methods involve the addition of excess lead-iodide ( $\text{PbI}_2$ ) during the sample preparation or treating the samples with methylammonium iodide and potassium acetate [31, 32]. For the main measurements in this thesis, the materials will be kept either under nitrogen or under vacuum, but in general, humidity intolerance is preferably avoided to enhance widespread application. The second issue, that of light-induced phase segregation, implies that under intense illumination the homogeneously mixed distribution of halides will segregate into iodide, and bromide-rich regions [33]. The phase segregation affects the charge-carrier dynamics in the material since the smaller-bandgap iodide-rich regions act as sinks for mobile charge-carriers. This means that charge-carriers will recombine more often in these areas, leading to an increase of the photoluminescence (PL) intensity and a red-shift of the PL peak position, due to the lower energy gap [34]. There exists, however, a photoexcitation intensity threshold for this ion diffusion, and by moderating the illumination intensity, this phase segregation can be avoided [35]. For experimental methods which include the illumination of the sample, a way to confirm the light-stability under the used intensity is to measure the PL emission before and after a period of illumination and one can check whether or not the results of the experiment match.

When considering these remaining stability difficulties, the overall device stability of the all-inorganic PSC is improved compared to its organic-inorganic counterpart, but in terms of the PCE, this type of material is lacking with its maximum value being only two-thirds of the current PCE record-holding PSC [20]. In the next section the incorporation of the perovskite layer into a full device will be discussed.

## 2.2 Perovskite solar cells

To understand more about the role of the perovskite material as an active photovoltaic layer in a PSC, the configuration of the device used in this thesis will be explained paired with the corresponding band diagram.

The  $\text{CsPbI}_2\text{Br}$  perovskite absorber layer with a bandgap of  $E_g \approx 1.9 \text{ eV}$  is used in a PSC, built in the inverted planar p-i-n structure. The device structure with the corresponding band diagram is shown in Figure 4.

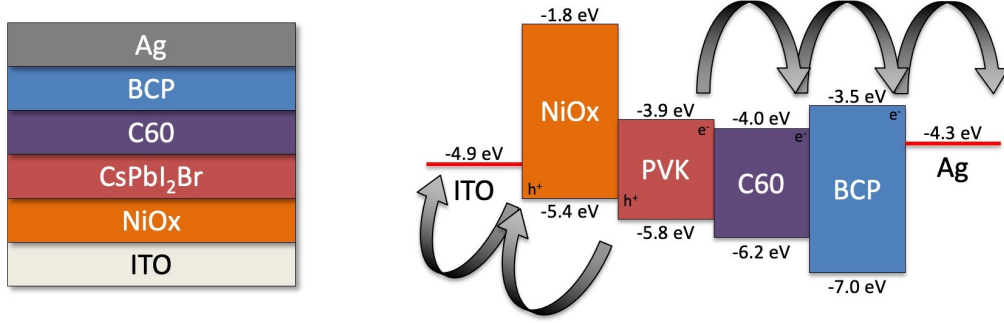


Figure 4: left: A schematic overview of the PSC planar structure. right: A schematic overview of the band diagram of the PSC with the direction of the charge-carrier movements [36, 37, 38, 39, 40, 41].

In Figure 4 starting in the device structure from the bottom, indium tin oxide (ITO) serves as the transparent conducting oxide bottom contact. On top of the anode, a layer of p-type nickel oxide (NiOx) is deposited. This metal oxide functions as the hole transport layer (HTL) inside the cell. The solution-processed  $\text{CsPbI}_2\text{Br}$  perovskite thin film is the photoactive layer of the device. As the electron transport layer (ETL), the n-type  $\text{C}_{60}$  is evaporated onto the perovskite layer. In between the silver (Ag) metal contact and the ETL, a thin layer of bathocuproine (BCP) is evaporated, which creates an ohmic contact between the transport layer and the cathode. Without the BCP layer, a small Schottky barrier between the  $\text{C}_{60}$  and Ag would form, leading to an accumulation of charges. The thickness of the BCP hole blocking layer must be kept low since otherwise the tunnelling path of the electrons will be too long and no charges will pass [42].

### p-n junction

For the analysis of the capacitance-based measurement method of DLTS on the described PSC device, several assumptions are made, such as the formation of a p-n junction between the light p-type perovskite layer and the strong n-type ETL  $\text{C}_{60}$  [43], while the type of doping for both materials is still the topic of ongoing debate. In the case the assumption holds, a schematic representation of such a junction is shown in Figure 5, where the n-type material is on the left side and the p-type on the right.

In Figure 5 both the VB and CB energy levels, denoted as  $E_V$  and  $E_C$  respectively, are drawn over the formed p-n junction, with the constant Fermi level  $E_F$  throughout the junction that is formed upon connecting the two layers. At the p-n junction a depletion region forms, which is depleted of free charge carriers due to the internal electric field that causes the charges to drift away. The width of this depletion region is denoted by  $w$ , with a contribution in the n-type material  $w_n$  and a broader part in the p-type material  $w_p$ . The stronger doping of the n-type material is visualised by the reduced energy difference between  $E_C$  and  $E_F$  compared to the difference between  $E_V$  and  $E_F$  in the p-type material.

### One-sided abrupt junction assumption

The depletion region shown in Figure 5 is distributed unevenly over the two materials and this has to do with the large difference in the doping concentrations in both materials. To preserve charge neutrality, the following equality must hold:  $N_D w_n = N_A w_p$ , where  $N_D$  and  $N_A$  are the amount of charges present in the depletion region in the n-type and p-type



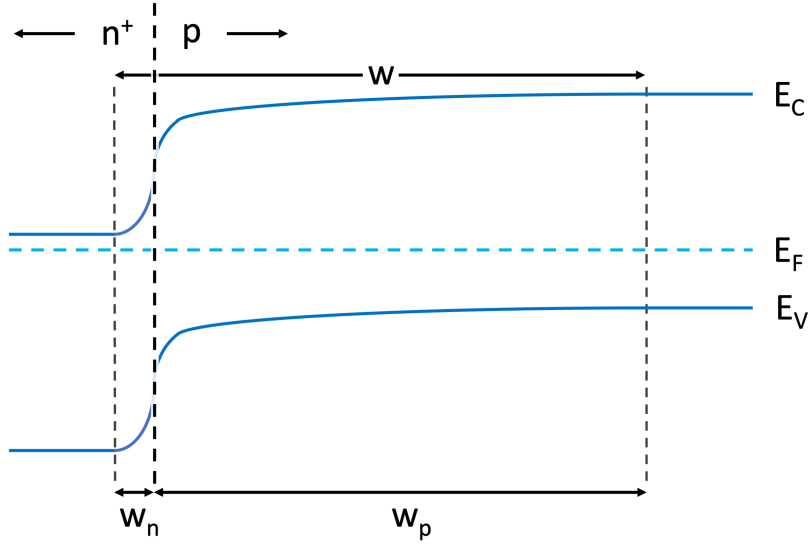


Figure 5: Schematic overview of a p-n junction formed between a strong n-type material and a low-doped p-type material.

materials respectively. Due to  $N_D \gg N_A$ , the width of the SCR inside the p-type material far exceeds the width inside the n-type  $w_p \gg w_n$ . The one-sidedness of this p-n junction leads to the labeling of such a junction as a one-sided abrupt (OSA) junction. For the DLTS measurements the OSA junction assumption is applied, which states that the change in the depletion region width is primarily happening inside the p-type material.

As mentioned before, the SCR is depleted of charges due to the internal electric field and as a result, charges will accumulate on either side of the SCR and the junction can in this way be approximated as a parallel-plate capacitor, where either side holds charges separated by the depletion layer width, with a potential difference in between them. Due to the OSA junction approximation, the probing of the change in depletion capacitance reveals information about the p-type material, since this is assumed to make up the majority of the SCR. In Section 2.5 on the method of DLTS, this approximation will be expanded on and how this can be used to extract information on the charge carrier dynamics in the material. First, it is essential to discuss the latter and explain which pathways photogenerated charges can follow and how these are affected by defects in the material and by changes in temperature.

## 2.3 Charge-carrier and recombination dynamics

### Photogeneration of free charge-carriers

For a photon to be absorbed by a photoactive absorber layer, the photon energy must be equal to or larger than the bandgap energy. In the case of CsPbI<sub>2</sub>Br, only photons with an energy  $E_g \geq 1.9$  eV will be absorbed, which corresponds to photons with wavelengths  $\lambda \leq 652$  nm. In this process, an electron-hole pair is formed, by exciting an electron from the VB to the CB. For perovskites, it is believed that initially these charges are not directly free, but form an exciton, which is a bound state of a hole polaron and an electron polaron [44]. However, since the exciton binding energy of around  $E_B = 22$  meV is comparable to the thermal energy present at RT,  $E_{th} \approx 26$  meV, these excitons will break apart and free charges will be created [45]. This fact is one of the main contributors to the high photovoltaic efficiency of perovskites since the yield of mobile charge generation from photon absorption is almost equal to unity at room temperature.

In a perovskite thin film, the breaking of the exciton bonds will lead to mobile holes and electrons in the valence and conduction band respectively. All of these charge carriers will recombine eventually after being generated, such that the charge balance is preserved. Before recombining the dynamics of the charge carriers inside the electronic bands can be expressed by the diffusion length  $L_D$ , which is the average distance a charge-carrier moves between generation and recombination. The latter can be calculated as shown in Equation (1),

$$L_D = \sqrt{\frac{k_B T}{e} \mu \tau} \quad (1)$$

where  $k_B$  is the Boltzmann constant,  $T$  is the temperature of the material,  $e$  is the elementary charge,  $\mu$  is the mobility, which tells how fast a charge-carrier can move through the material in the presence of an electric field and  $\tau$  is the lifetime, which is the time between the generation and recombination of a mobile charge-carrier [46]. How these values change over temperature will be discussed later in this section, but first, we will discuss the possible pathways of the charge-carriers from generation to recombination and how these affect the lifetime of such a charge-carrier.

### Band-to-band recombination

The most direct way of recombination is radiative band-to-band recombination, where an electron near the conduction band minimum (CBM) recombines with a hole near the VBM while emitting a photon with an energy corresponding to the energy difference between the two bands [46]. However, there are multiple processes that cause non-radiative recombination competing with this radiative band-to-band recombination. One of these non-radiative pathways can also be considered as direct recombination, the physical origin of which is still a topic of debate and this type of non-radiative decay will be addressed in the section on temperature-dependent charge-carrier dynamics. First, the non-radiative trap-assisted recombination will be discussed.

### Trap-assisted recombination

In an ideal semiconductor, there are no allowed states with an energy inside the bandgap and in this type of material, only direct recombination would be possible. In reality, however, there are many of these intermediate bandgap energy states [46]. These states are caused by defects in the material, which come in a relatively high concentration in perovskites due to the solution-based low-temperature processing [47]. The defects come in different forms, such as point defects formed by atomic vacancies, interstitials and by anti-site atomic substitutions or defects with a higher dimensional shape formed by local lattice dislocations and grain boundaries (GBs) [47]. Each of these defect types has a certain energy state, also called a trap state, which we can divide into states close to the band edges called shallow traps (STs) and deep traps (DTs) with an energy level close to the midgap energy level. The latter type of trap is the most efficient in mediating non-radiative recombination in comparison with shallow traps [48]. The recombination process through DTs is described

using the Shockley-Read-Hall theory of trap-assisted recombination and these trap states are usually formed by higher dimensional defects, such as GBs [49, 47]. Since these trap states increase the non-radiative recombination of mobile charge carriers, the lifetime and thus the diffusion length of these carriers is reduced significantly. A high concentration of defects that cause DTs will diminish the photovoltaic performance of a semiconductor, thus in that sense, it is surprising that a solution-processed material can have such outstanding photovoltaic efficiencies. An explanation for this apparent 'defect tolerance' of the perovskite layer, is that a large fraction of the defects consists of point defects. These point defects often have an energy level that lies either inside or near the respective energy bands, with the latter type creating the energetically favourable STs [48]. Defects with energy levels outside of the bandgap do not form intermediate-band trap centres, thus not affecting the charge-carrier dynamics through trap-assisted non-radiative recombination and the presence of these passive defects significantly contributes to the defect tolerance of a material. Since STs have an energy level relatively close to the edges of the bandgap, this type of trap is less efficient in mediating non-radiative recombination than a DT, while the probability of the emission of a charge carrier back in its respective energy band is far greater. After emission a hole or an electron will again be mobile in the valence or conduction band respectively, thus the recombination or annihilation is delayed and the lifetime of the charge-carrier is prolonged. Other studies however suggest that there actually is a significant concentration of DTs present, but due to the anharmonicity in the crystal structure the trap-assisted recombination via these DTs is limited [48].

Besides the fact that the trap-assisted recombination is limited for a fraction of the deeper traps, a high concentration of DTs will still enhance the non-radiative recombination. In a solution-processed perovskite thin film, which has a polycrystalline nature with a certain structural disorder, these DTs are highly concentrated on the GBs. Improving the crystallinity of the material using a treatment and thus reducing the amount of GBs has proven to lengthen the charge-carrier lifetime [50].

Another favoured location of defect formation is at the surface of the perovskite film since perovskites have a very unstable and reactive surface due to dangling bonds [51]. This is especially noticeable in a PSC, where the perovskite layer interfaces charge-transport layers. In this situation a mismatch of atomic orbitals is present and a way to solve this issue is by passivating the surface [52]. For the PSC device shown in the previous section, this surface passivation will increase the charge extraction at the electrodes, since a smaller fraction of the generated charge carriers will recombine non-radiatively before reaching the contacts. This charge-extraction is the additional possible pathway for mobile charge carriers, compared to an isolated perovskite layer, which is made possible by the internal electric field of the formed SCR. Electrons that are generated in the depletion region will drift through the ETL, while mobile holes will drift through the strong p-type HTL, and by reaching the contacts a current will establish. The charge extraction can be improved by improving the alignment of the band energies between the perovskite and the transport layers. However, in all-inorganic perovskite layers relatively low values for the open-circuit voltage ( $V_{OC}$ ) and the short-circuit current density ( $J_{SC}$ ) are reported, the former of which is assumed to originate from the high amount of non-radiative recombination losses [29]. The probing of these loss mechanisms is thus essential for the improvement of the PSC performance. Before discovering how to probe the charge-carrier dynamics in both a single perovskite layer and in a PSC at different temperatures, the temperature dependence of the physical processes behind the dynamics will be discussed.

### 2.3.1 Temperature-dependent charge-carrier dynamics

#### Photoluminescence

The first process after the photogeneration of an electron-hole pair is the dissociation of the formed exciton. For this to happen, the thermal energy of the system must be sufficiently high to break up the exciton binding. Despite the exciton binding energy being relatively low in this perovskite material, this condition may not hold for the entire range of measured temperatures [45]. For the TRMC measurements, the generation of free charge carriers is necessary to measure a signal, but PL offers a method to investigate both excitons and free charges since both can recombine radiatively. The literature on PL measurements both shows

that metal halide perovskites have a thermally activated blueshift and an intensity decrease of the PL emission peak [53]. The blueshift indicates narrower bandgap energy at lower temperatures, which is believed to have its origin in the combination of lattice expansion and electron-phonon coupling in the material [54]. The exact origin of the increased PL emission at lower temperatures is still a topic of ongoing debate. Before discussing the existing arguments, the yield of the PL emission  $\phi_{\text{PL}}$  is defined in Equation (2),

$$\phi_{\text{PL}} = \frac{k_{\text{r}}}{k_{\text{r}} + k_{\text{nr}}} \quad (2)$$

where  $k_{\text{r}}$  is the radiative component of the direct-recombination rate and  $k_{\text{nr}}$  is the non-radiative component of this direct recombination rate, which will in the next Section 2.4 be denoted by  $k_2 = k_{\text{r}} + k_{\text{nr}}$ . For the PL yield to go up significantly the ratio in Equation (2) must increase at lower temperatures, which can be achieved by a thermally activated direct non-radiative recombination component  $k_{\text{nr}}$ . Arguments given in the literature for the thermally activated nature of  $k_{\text{nr}}$  is the occurrence of Rashba splitting between the CBM and VBM after photo-generation of charge carriers [55]. Due to this displacement in k-space, it is physically impossible to directly recombine radiatively. Instead, the direct recombination happens non-radiatively upon interaction with phonons present in the material, which makes this a thermally activated process. In the case of a direct-bandgap material, non-radiative multiphonon recombination is possible as well, but that is an unlikely recombination pathway compared to the other types of non-radiative recombination [56]. Other explanations given for the increased PL emission intensity at lower temperatures is due to less available thermal energy to break up the exciton bonds and lower activation energy for radiative recombination due to the diminished interference of traps [57, 58].

In time-resolved PL (TRPL) measurements the transient of the PL emission can be investigated and the temperature-dependence of the PL emission decay depends on the excitation intensity used. At low excitation intensities, trap-assisted recombination will dominate the charge-carrier dynamics and as we will discuss later in this section this process is thermally activated [59]. For higher intensities, however, the direct band-to-band recombination will dominate, a process that is thermally reduced, so the higher temperatures will have the slowest decays. This reduction in the recombination rate at higher temperatures has to do with the spreading of the Fermi-Dirac distribution function, which leads to a widening of the thermal energy range of the charge carriers in their respective energy bands [59].

## Mobility

In case the excitons dissociate, the free charge carriers move in their respective energy band at a certain velocity, defined by the electronic mobility  $\mu$ . The limiting factor of the mobility is the scattering of the mobile charge carriers with acoustic phonons. The number of phonons will increase when the material gets more thermally excited, reducing the mobility. The value of the mobility in perovskites is inversely proportional to the temperature as  $\mu \propto T^{-\alpha}$ , where the value of  $\alpha$  typically ranges from  $1.3 < \alpha < 1.7$ , but some have reported values up to  $\alpha = 2.8$  [60, 61]. At very low temperatures this relation may not hold anymore, and a possible explanation for this is that a phase transition can occur from the cubic perovskite structure to the tetragonal phase [59].

## Dynamics of defect levels

In the perovskite material, defects can form with energy levels inside the bandgap. These intermediate band trap centres can mediate non-radiative recombination of the charge carriers and the temperature-dependent dynamics of which will be discussed in this section. The formation and mobility of point defects are thermally activated, but the trapping, emission and recombination rates through these defects all have a different temperature dependence [62]. First off, the trapping rate of a mobile charge-carrier by a trap state is thermally activated as it increases by one order of magnitude when heating from several tens of Kelvin to room temperature. This is because it follows the trend of increased defect formation [63]. When a charge carrier is trapped, the emission rate of the trapped charge carrier back to the respective energy band is determined by both the energy difference between the two energy

states and the temperature of the system. Following Shockley-Read-Hall defect statistics, the thermal emission rate for electron traps is given by Equation (3),

$$k_E = \frac{1}{\tau} = \sigma_n \nu_{th} N_C \exp\left(-\frac{E_T}{k_B T}\right) \quad (3)$$

where  $\sigma_n$  is the electron capture cross section,  $\nu_{th}$  is the thermal velocity,  $N_C$  is the density of states in the conduction band,  $E_T$  is the depth of the electron trap centre from the conduction band,  $k_B$  is the Boltzmann constant and  $T$  is the temperature. The prefactor of the exponent can be simplified to a function of temperature by using that  $\nu_{th} \propto T^{\frac{1}{2}}$  and  $N_C \propto T^{\frac{3}{2}}$ . The capture cross section  $\sigma_n$  is shown to depend on the temperature in an exponential manner, with the depth of the trap defining the Boltzmann factor as  $\sigma_n \propto \exp -\frac{E_T}{k_B T}$  [64]. Including these temperature dependencies yield the following expression for the thermal emission rate,

$$k_E = A(T) \exp\left(-\frac{2E_T}{k_B T}\right) \quad (4)$$

where  $A = A_0 T^2$  is the attempt-to-escape frequency [49]. An argument for the hole thermal emission rate can be made analogously.

For the trap-assisted recombination rate, both SRH statistics and experimental data show that this non-radiative recombination is thermally activated [49, 59]. In terms of charge-extraction by the transport layers, literature shows that the charge transport is reduced at lower temperatures, diminishing the photovoltaic efficiency at lower temperatures [65]. However, for the thesis, we will only focus on the charge-carrier dynamics inside the photoactive layer. The probing will be performed using two different methods, namely time-resolved microwave conductivity (TRMC) measurements and deep-level transient spectroscopy (DLTS), which will be elaborated on in the following two sections.

## 2.4 Time-Resolved Microwave Conductivity

The time-resolved microwave conductivity (TRMC) method is based on the microwave absorption of photo-induced mobile charge carriers. In a TRMC experiment, both the lifetime and the mobilities of these mobile charge carriers can be extracted from the measurements done on the material, which is the all-inorganic mixed-halide  $\text{CsPbI}_2\text{Br}$  perovskite thin film in the case of this thesis. An important feature of this method is that it does not require the fabrication of a full solar cell device, a process that can affect the photoactive material. Another advantage of this non-invasive measurement method is that it can reveal information on the charge-carrier recombination, both radiative and non-radiative, while an alternative method like time-resolved photoluminescence (TRPL) only accounts for the radiative recombination. Since the effect of defects on the charge-carrier dynamics is the research subject of this thesis and that trap-assisted recombination is non-radiative, the TRMC method is especially useful. First, the measurement setup will be shown, followed by the physics behind the analysis and the kinetic model used to fit the measured data.

### Experimental setup

A schematic overview of the TRMC-setup used in this thesis is shown in Figure 6, where Figure 6a on the left shows the global setup and Figure 6b shows a close up of the cell in which the sample is placed.

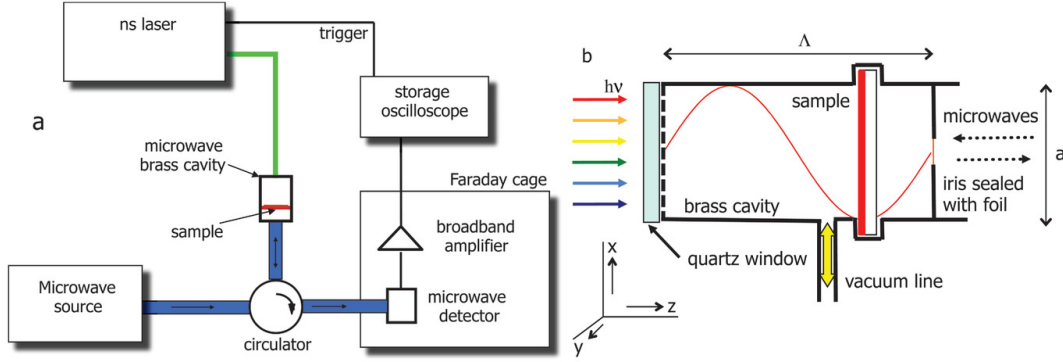


Figure 6: a. A schematic overview of the TRMC-setup. b. A schematic overview of the microwave cell containing the sample. Figure taken from ref. [66].

The sample, shown in Figure 6b, is photoexcited by a laser pulse, while simultaneously being radiated by microwaves coming from a microwave source. The sample is placed inside a gold-plated waveguide cell fitted with a metal grating that allows the incoming excitation light to pass through, while fully reflecting the microwaves, sealed off from ambient exposure with a quartz window. Due to the placement of the sample inside the cell, the photo-excited charges interact with the incoming microwaves at the maximum intensity point of the electric field. This cell can be equipped with an iris, causing a standing wave inside the cell, which increases the interaction of the microwaves with the charges in the sample. This increased sensitivity allows for lower photoexcitation intensities to be used, but it comes at the cost of a reduced time resolution. A cell with or without the iris is called a cavity cell or an open cell respectively. The attenuated microwaves leave the cell and are separated from the incoming waves by a circulator, travelling to a diode detector inside a Faraday cage. The incoming microwaves get converted into current by the detector and an offset regulator is used to subtract the DC part of the signal, leaving the AC signal which arises from the attenuation. Since this is only a small fraction of the incoming current, the AC signal is amplified before being recorded over time and stored on an oscilloscope. Each laser pulse triggers a measurement of the oscilloscope through an optical sensor, which is subsequently averaged to obtain clean traces.

### Governing equations

The laser pulse generates mobile charge carriers in the perovskite material, increasing the conductivity of the semiconductor material as described by equation (5).

$$\sigma = e \sum_i n_i \mu_i \quad (5)$$

Here the electric conductivity  $\sigma$  is determined as the elementary charge  $e$  multiplied with the product of the concentration of mobile charge carriers  $n$  and their mobility  $\mu$ , summed over each type of charge carrier. When integrating the change in conductivity  $\Delta\sigma$  over the sample thickness, one can extract the change in conductance of the sample, as shown in equation (6).

$$\Delta G = \beta \int_0^L \Delta\sigma(z) dz \quad (6)$$

Where  $\Delta G$  is the change in conductance,  $L$  denotes the material thickness and  $\beta$  is a geometric ratio between the respective height and width of the sample. From this relation, it follows that the change in the charge-carrier concentrations and mobilities will change the conductance of the sample. This is useful since the change in conductance is related to the attenuation of the microwave power during a TRMC measurement as given by equation (7).

$$\frac{\Delta P(t)}{P} = -K \Delta G(t) \quad (7)$$

Where  $\Delta P(t)$  is the change in microwave power over time,  $P$  is the unperturbed microwave power,  $K$  is a sensitivity factor and  $\Delta G(t)$  is the change in conductance over time. The microwaves cause the charge to drift over a small distance due to the oscillating and low magnitude electric field of the waves. These slight displacements however still cause a reduction of the microwave power and the higher the change in conductance, the higher the attenuation of the microwave power will be. By measuring this over time, one can extract information about the mobility, concentration and lifetime of photoexcited charge carriers.

To measure and compare different types of material and using different types of cells, equation (5) is rewritten as

$$\sigma = en(\mu_e + \mu_h) \quad (8)$$

The yield  $\phi$  is introduced as follows, assuming that every absorbed photon creates an electron-hole pair

$$\phi = \frac{Ln}{F_A I_0} \quad (9)$$

With  $L$  the sample thickness,  $n$  the concentration of electron-hole pairs,  $F_A$  the fraction of absorbed light and  $I_0$  the intensity of the incoming laser pulse given as photons per pulse per unit area. When combining equations (8) and (9) and rewriting in terms of the change in conductance, one finds the following relation

$$\phi(\mu_e + \mu_h) = \frac{Ln}{F_A I_0} \frac{\Delta\sigma}{en} = \frac{L}{F_A I_0} \frac{\Delta G_{max}}{e\beta L} = \frac{\Delta G_{max}}{F_A I_0 e\beta} \quad (10)$$

Since the last term in equation (10) is normalised for the geometry of the sample  $\beta$ , the fraction of absorbed photon  $F_A$  and the incoming laser intensity  $I_0$ , the measurements can be analysed and compared for different types of materials.

### Kinetic model

In the previous section, it was shown how to express the microwave power attenuation over time into the development of the charge-carrier dynamics of the material. Here, a kinetic model is presented that is used to fit the measured traces and to extract actual physical



parameters of the material from the TRMC measurements. The model quantitatively describes multiple recombination pathways for the photogenerated mobile holes and electrons. The validation of this model will be presented in the results section when combining the results from both TRMC and DLTS. The processes in this kinetic model are shown in Figure 7.

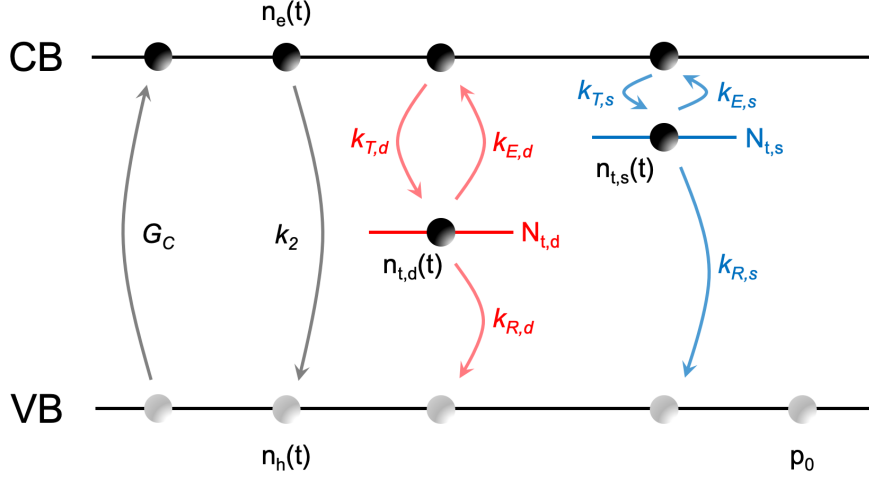


Figure 7: Kinetic model presented in a schematic band diagram of the perovskite material upon photoexcitation.

In Figure 7 a band diagram is shown, where mobile charge carriers, namely electrons and holes, are generated by a laser pulse. The photoexcitation leads to a generation rate, described by  $G_C$ , creating mobile conduction band (CB) electrons and valence band (VB) holes at concentrations  $n_e(t)$  and  $n_h(t)$  respectively. These concentrations are time-dependent since the charges can recombine through multiple pathways. In the Figure the direct recombination rate  $k_2$  is shown first. As described in Section 2.3.1, this direct recombination term is assumed to consist of a radiative  $k_r$  and a non-radiative part  $k_{nr}$ , such that  $k_2 = k_r + k_{nr}$ . In addition to this direct recombination, there are two electron traps, with concentration  $N_{t,i}$ , present that can trap mobile CB electrons at a certain rate  $k_{T,i}$ . The trapped electrons, at density  $n_{t,i}$ , can be either thermally emitted back to the CB at rate  $k_{E,i}$  or recombine non-radiatively with VB holes at rate  $k_{R,i}$ . In this model the assumption is made that there are 'deep' traps present and 'shallow' traps at concentrations  $N_{t,d}$  and  $N_{t,s}$  respectively. The depth of the trap is defined by the energy difference between the trap energy level and the CB energy level, which is larger in the case of the deep trap. This leads to a lower emission rate,  $k_{E,d} < k_{E,s}$ , and capture rate,  $k_{T,d} < k_{T,s}$ , but a higher relative trap-assisted non-radiative recombination rate  $k_{R,d} > k_{R,s}$ . No initial relative constraints are set for the respective concentrations of both traps. For both direct and trap-assisted recombination, the electrons can recombine both with the generated VB holes, but additionally with the holes that are present due to the intrinsically p-doped nature of the perovskite material, with density  $p_0$ .

This kinetic model is governed by four coupled ordinary differential equations (ODEs), which describe the time-dependent concentrations of  $n_e(t)$ ,  $n_h(t)$ ,  $n_{t,d}(t)$  and  $n_{t,s}(t)$ , where the latter two describe the concentrations of trapped electrons in the deep and shallow traps respectively.



$$\frac{dn_e}{dt} = G_C - k_2 n_e (n_h + p_0) - k_{T,d} n_e (N_{t,d} - n_{t,d}) + k_{E,d} n_{t,d} - k_{T,s} n_e (N_{t,s} - n_{t,s}) + k_{E,s} n_{t,s} \quad (11)$$

$$\frac{dn_h}{dt} = G_C - k_2 n_e (n_h + p_0) - k_{R,d} n_{t,d} (n_h + p_0) - k_{R,s} n_{t,s} (n_h + p_0) \quad (12)$$

$$\frac{dn_{t,d}}{dt} = k_{T,d} n_e (N_{t,d} - n_{t,d}) - k_{E,d} n_{t,d} - k_{R,d} n_{t,d} (n_h + p_0) \quad (13)$$

$$\frac{dn_{t,s}}{dt} = k_{T,s} n_e (N_{t,s} - n_{t,s}) - k_{E,s} n_{t,s} - k_{R,s} n_{t,s} (n_h + p_0) \quad (14)$$

For a given set of parameter values, an ODE solver is used to calculate the time-dependent concentrations. Using equation (15), the change in conductance  $\Delta G(t)$  can be calculated from the solutions for the time-dependent concentrations.

$$\Delta G(t) = e(n_e(t)\mu_e + n_h(t)\mu_h)\beta L \quad (15)$$

For the calculation, it is assumed that only mobile charge carriers, described by equations (11) and (12), contribute to the conductance of the material. Thus the trapped electrons, governed by equations (13) and (14), do not contribute due to their immobile nature and the doping charge concentration  $p_0$  does not contribute since this value remains constant. Since the change in conductance is calculated by summing over all charge carriers, this means that the origin of the measured intensity might only come from mobile holes. This is the case for relatively low excitation intensities when the photoexcited CB electrons get immobilised by the trap states, and only mobile holes remain. In the case of high illumination intensity, the concentration of charge carriers will exceed the number of trap states and direct recombination will dominate the dynamics. In the results section, both these domains will be elaborated on further. Using equation (10) and (15), the solutions from the ODE can be compared to the actual measurements and the set of parameters can be optimised for the fitting of the measured traces. An important note for the kinetic model and the corresponding set of ODEs is that the whole system can be rewritten by switching the negative and positive charge carriers, without affecting the resulting change in conductance over time. The experiment itself is not able to distinguish between the two cases, thus the type of excess charges and charge-carrier traps is assumed.

Further assumptions made are that the mobility values of the charge carriers are constant during the short time period of measurement and that these charges are generated and decaying in a homogeneously distributed fashion across the material. The latter assumption holds if the excitation wavelength is chosen fairly close to the absorption onset of the material. Another key assumption is that the electron-hole pair dissociation quantum yield is assumed to be unity. This is a valid argument since the exciton binding energy in the perovskite material is lower than the thermal energy present, causing each electron-hole pair to dissociate into a mobile CB electron and VB hole.

## 2.5 Deep-Level Transient Spectroscopy

### Capacitance of PSC device

The next method that will be used to investigate the effect of the defect landscape on the charge-carrier dynamics in the all-inorganic mixed-halide perovskite thin films is deep-level transient spectroscopy (DLTS). This capacitance-based method was first introduced by D.V. Lang in 1974 as a method to probe trap states in semiconductor materials [67]. In contrast to the TRMC method, which only requires a perovskite thin film, in DLTS a complete solar cell is characterised, details of which were discussed in Section 2.2. To explain the working mechanism behind this method, we will return to the theory of Section 2.2, where the formation of an SCR at the interface between a p-type perovskite and a strong n-type ETL was discussed. It was mentioned that the accumulation of charges on either side of the SCR lead to the approximation of the depletion layer as a parallel plate capacitor. Using the OSA junction approximation, we assume that this depletion layer is almost entirely in the low-doped perovskite layer [46]. Now we will express this depletion layer capacitance  $C_{\text{dl}}$  as follows.

$$C_{\text{dl}} = \frac{\varepsilon \varepsilon_0 A}{w_{\text{D}}} \quad (16)$$

with  $\varepsilon_0$  the vacuum permittivity,  $A$  the active area of the material,  $w_{\text{D}}$  the depletion region width and  $\varepsilon$  the dielectric permittivity from the material [68]. The depletion region width  $w_{\text{D}}$  in equation (16) takes a certain value in equilibrium, but it can be altered by applying a bias voltage, as described in equation (17).

$$w_{\text{D}} = \sqrt{\frac{2\varepsilon_0\varepsilon}{qN}(V_{\text{bi}} - V)} \quad (17)$$

By applying reversed bias,  $w_{\text{D}}$  is widened, where  $N$  is the number of charges present inside the depletion region. From equation (16) follows that the widening will lead to a drop in the capacitance.

### Measurement working principles

The other way around, the depletion width can be fully collapsing, by applying a sufficient forward bias. The reduction of  $w_{\text{D}}$  increases the capacitance  $C_{\text{dl}}$ , as is the case during the DLTS measurements. A schematic overview of the proceedings in a DLTS measurement is shown in Figure 8.

In Figure 8a the system is in equilibrium as the first step, where the p-n junction yields a certain depletion region width. During the second step, shown in Figure 8b, charge carriers are injected by a DC forward bias pulse, which causes the depletion region width to collapse and leads to an increase in the capacitance. The presence of mobile charge carriers in this region, previously depleted, allows for the electronic trapping of these charge carriers into intermediate band trap states, which in the case of Figure 8 are electron traps [67]. The injection pulse is saturating, which means that the pulse is strong and long enough for a complete filling of the electronic traps. An injection pulse width in the order of milliseconds is already sufficient for the saturation, due to the fast trapping rates of the electronic defects [68]. By using filling pulses in the order of seconds, not only electronic charges but also ionic movement will influence the capacitance of the system, which is the topic of transient ion-drift (TID) measurements [68]. In the third and final step in Figure 8c, the bias pulse is removed and this causes the broadening of  $w_{\text{D}}$ , but its equilibrium value will not directly be obtained. This is due to the presence of trapped charge carriers that prevent the region to be depleted of charges. When the electrons are emitted from the electronic traps, the number of charges in the depletion region will be reduced. Since the product of the depletion region width and the number of charges must be equal on either side of the p-n junction, a reduction in charge leads to an increase in the width and thus a reduction in the capacitance in the form of a decaying transient. In the case of majority-carrier traps, holes will be emitted from the electronic traps after removing the bias pulse. The hole-emission process will lead

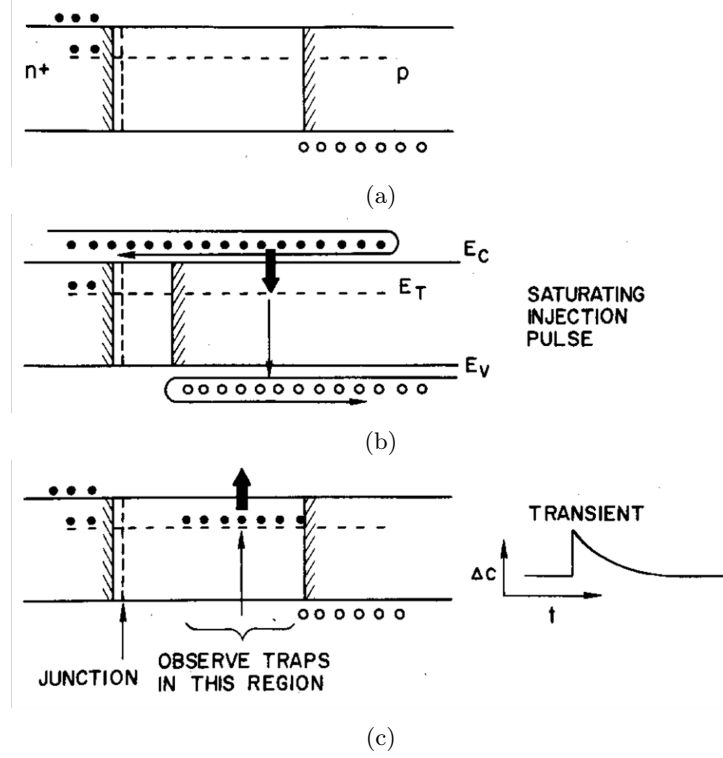


Figure 8: Schematic overview of the DLTS measurement cycle, reproduced from [67].

to more electrons inside the depletion region, thus increasing the charge. Using the same argument as for the minority-carrier traps, the increase in charge will decrease the depletion region leading to a rising transient of the capacitance. Only after the thermal emission of the charge carriers back to their respective energy band, the carriers are mobile again and able to move out of the SCR. After the traps are emptied the depletion region width will return to its equilibrium value, leaving the system the same as in the first step of the DLTS cycle. Since the mobile opposite charges have already moved out of the SCR due to the internal field, the trap-assisted non-radiative recombination rate is diminished significantly and the capacitance transient is thus caused by thermal emission from the trap states. A rising transient is assigned to the emission from majority traps, while decay is believed to originate from minority traps. Which type of charges can be assigned to each respective type of trap state, depends on the assumption whether the material is p-type or n-type. Furthermore, there exists a detection threshold of the defect concentration, since charges should affect the electrostatic potential distribution across the p-n junction sufficiently [69]. This detection threshold is thickness dependent and for thin-film materials, the minimum concentration of defects should exceed  $N_{def} \geq 10^{16} \text{ cm}^{-3}$ . This number consists of both the doping defects and the defects that affect the minority carriers.

The carrier emission happens at a certain rate, described by Equation (4) and this causes a certain change in capacitance over time. By measuring the capacitance transient over multiple temperatures, activation energy can be derived by making an Arrhenius plot and using equation (4), which makes a comparison with the TRMC measurements possible, as will be discussed in Section 5. If the capacitance transient can be assigned to the emission of an electronic trap state following Shockley-Read-Hall statistics, this activation energy will correspond to the energy difference between the trap energy level and the energy level of the respective energy band. The concentration of the defects that cause the transients can be linked to the change in capacitance [68].

### Probing of capacitance transients

The probing of the capacitance transient is done by applying an AC bias voltage, with an amplitude much lower than the DC bias pulse, and simultaneously measuring the current

response. Using this current response, the complex impedance  $Z$  is calculated as in equation (18).

$$Z(t) = \frac{V_0 \sin(\omega t)}{I_0 \sin(\omega t + \Phi)} = Z_0 e^{-i\Phi} = Z' - iZ'' \quad (18)$$

Where  $V_0$  and  $I_0$  are the amplitudes of the applied voltage and current response respectively,  $\omega$  is the frequency of the AC voltage bias and  $\Phi$  is the phase delay between the voltage input and the current response. To translate this complex impedance into a value of the capacitance  $C$ , a suitable equivalent circuit model (ECM) must be chosen. For the instrument system, the ECM includes next to the capacitor both a parallel and a series resistance, which makes the calculations for the capacitance value incredibly cumbersome. In order to make the latter easier, the series resistance must be eliminated from the ECM. Neglecting the contribution of the series resistance is valid when the phase delay of the current response is at  $-90^\circ$ . Using thermal admittance spectroscopy (TAS) one can measure this phase delay over a set range of AC probing frequencies. Typically, for a PSC device, a probing frequency of  $\omega = 10$  kHz yields a phase delay around the desired value. When neglecting the series resistance the complex capacitance can easily be calculated using Equation (19).

$$C^*(\omega) = (i\omega Z)^{-1} \quad (19)$$

### Fitting model

The resulting measured capacitance transient is fitted using exponential functions, with the general equation for the calculated capacitance  $C_f$  given in Equation (20).

$$C_f(t) = \sum_i [\Delta C_i \exp(-\frac{t}{c_i T \exp(\frac{E_{A,i}}{k_B T})})] + C(\infty) \quad (20)$$

The capacitance transient  $C_f(t)$  is fitted using the summation of exponential contributions. Each contribution consists of  $\Delta C_i$ , which yields the amplitude and sign of the transient,  $c_i$  which defines the change rate of the transient and  $E_{A,i}$  which is the activation energy of the respective process that causes the transient. Next to the summation of these exponentials,  $C(\infty)$  accounts for the steady-state capacitance values of the measured traces at each temperature. By using the differential evolution algorithm from the SciPy library, a fit is computed that matches the measured traces and the physical parameters such as the activation energy can be extracted [70]. The number of exponents needed may differ, depending on how many processes are causing the capacitance transient. In the Method Section 3.4, the used parameter ranges and the number of exponential contributions will be elaborated on.

## 2.6 Research question

Now that we have covered the theory behind both the material and measurement methods used in the thesis, it is time to combine all this into the research question for this thesis. The main goal of this thesis is to investigate the temperature dependence of the charge-carrier dynamics in all-inorganic mixed halide perovskite thin films and the effect of intermediate bandgap electronic trap levels on these dynamics. The two applied methods in this thesis, TRMC and DLTS, both reveal information on these dynamics with each their own working principle that carries particular advantages and limitations. The kinetic model used to analyse the TRMC measurements allows for the quantification of the concentration of traps and the trapping, emission and recombination rates that belong to the respective trap state. The fitting of the DLTS measurements reveals the activation energy for the electronic trap emission among others and this feature can be linked to the TRMC analysis. This is done by creating an Arrhenius plot using the emission rates from the TRMC measurements at different temperatures, which yields the activation energy for this emission process as the slope of the plot. By comparing the extracted activation energies of both methods, the possible matching of these values will make a strong argument for the validity of the applied kinetic model in the TRMC method and it will simultaneously be an indication that the electronic processes measured using the DLTS setup take place inside the perovskite material. The processes are in that case similar for the plain absorber layer compared to the one incorporated in a PSC device. Before making this comparison, the characterisation of the material will be shown, including the PL measurements, and the results and its discussion for both TRMC and DLTS.

## 3 Methodology

### 3.1 Sample Preparation

#### 3.1.1 Perovskite Thin Film Preparation

Glass substrates were cleaned using liquid detergent before putting them in an ultrasonic bath with subsequently acetone, ethanol and isopropanol for 10 minutes each. The cleaning step was finalised by exposing the samples to ozone plasma for ten minutes. The 1.2 M CsPbI<sub>2</sub>Br precursor solution was prepared by dissolving 350.3 mg lead iodide (0.6 mmol PbI<sub>2</sub>), 278.7 mg lead bromide (0.6 mmol PbBr<sub>2</sub>) and 394.5 mg caesium iodide (1.2 mmol CsI) in 1.266 mL dimethyl sulfoxide (DMSO). The precursor solution was spin-coated onto the glass substrates at 500 RPM for 3 seconds and at 2500 RPM for 30 seconds. The spin-coated samples were left at room temperature for 15 minutes before being annealing subsequently at 42 °C for 4 minutes and at 160 °C for 10 minutes, before being cooled down immediately on a metal surface to room temperature.

#### 3.1.2 Device Fabrication

For the full device preparation, an ITO glass substrate was cleaned using the same steps as for the glass substrates, before evaporating a 10 nm nickel (Ni) layer on top. By annealing for 20 minutes at 450 °C, with a 20 min ramp and cooling down afterwards, a thicker nickel oxide (NiOx) layer was formed. On top of this, the perovskite layer was deposited following the method described in Section 3.1.1. To complete the device, 30 nm of C<sub>60</sub>, 8 nm of bathocuproine (BCP) and 100 nm of silver (Ag) were evaporated onto the perovskite layer in the given order.

### 3.2 Characterisation

#### 3.2.1 Structural Characterisation

The X-ray diffraction (XRD) patterns were obtained using a Brucker D8 diffractometer, using the Bragg-Brentano configuration with Co-K $\alpha$  ( $\lambda = 1.79$  Å) radiation. The measurement range was set from 5° to 50°, with an 0.025° increment step and a dwell time of 0.1 seconds.

The thickness of the perovskite layer was measured using a profilometer, applying a force of 2 mg and measuring at a speed of 20  $\mu$ m/s, while recording at 200 Hz.

#### 3.2.2 Optical Characterisation

The absorption spectra were obtained using a Lambda 1050 spectrophotometer by PerkinElmer. The samples were placed inside a holder to prevent ambient exposure and the total fraction of transmitted ( $F_T$ ) light was measured. The fraction of absorbed ( $F_A$ ) light was calculated as  $F_A = 1 - F_T$ , where a baseline measurement was taken with just the empty holder.

For both the PL emission spectra and the TRPL measurements, the Edinburgh LifeSpec spectrometer was used. This device is equipped with a single photon counter and the excitation source consisted of a 405 nm picosecond pulsed diode laser. The excitation energy was around  $I_0 = 1.2 \times 10^{12}$  photons/cm<sup>2</sup> with a repetition frequency of 1 MHz, while the TRPL measurements used a frequency of 100 kHz. The measurements were performed inside a holder to prevent ambient exposure. Additionally, a 550 nm filter was placed and the measurements were averaged five times. For the TRPL measurements, a 10k count limit was applied for each temperature, except for the highest two, where a 1k count stop was applied due to the lower signal.

#### 3.2.3 Device Characterisation

Current-voltage curves measured under 1 sun provided by the Oriel 92250A solar simulator and recorded using the Keithley 2636A measurement device. The measurement was performed in a holder to prevent ambient exposure during the measurements.

IV curves were measured using the Probe Station from -0.2 V to 1.5 V. CV measurements were performed using Fluxim Paios, while the TAS measurements were performed using the Semetrol setup that was used for the DLTS measurements as well.

### 3.3 TRMC

The sample was illuminated by a 500 nm laser pulse of  $4\pm 1$  ns full width at half-maximum (FWHM) at a repetition frequency of 10 Hz. The laser intensity can be varied between  $10^9$  and  $10^{15}$  photons  $\text{cm}^{-2}$  per pulse using a set of neutral density filters. The monochromatic microwaves with a frequency in the range of 8.2 to 12.4 GHz were generated using a voltage-controlled oscillator, with the resonance frequency varying from 8.658 to 8.686 GHz when going from room temperature to the lowest temperature of 90 K respectively. The samples were measured in both an open cell and a cavity cell, measuring the laser full power at each temperature step to have an accurate normalisation for the incoming excitation intensity. The measurements were averaged 100 to 700 times going from the highest to the lowest intensity per cell type respectively.

The traces were fitted by applying a differential evolution algorithm that solves the ODEs that govern the dynamics in the applied kinetic model for varying parameter values. The fitting algorithm was run for 50k iterations, saving the 50 runs with the lowest residual values. By averaging over these 50 runs, the fitting parameters were extracted and used for the analysis of the measured traces.

### 3.4 DLTS

Using the capacitance measurement setup by Semetrol, a bias pulse of 1.4 V was applied to the pixels with a filling pulse width of 10 milliseconds and 1 second for the DLTS and TID respectively. A probing frequency of 10 kHz was used with an amplitude of 20 mV. The measurement temperatures ranged from 210 K to 330 K with an 8 K increment. For the lowest temperature, a stabilisation time of 10 minutes was used, while during the increasing steps each temperature was stabilised for 1 minute.

For the fitting of the capacitance transient a differential evolution algorithm was applied that solves Equation (20) for varying parameter values using two exponential contributions.

## 4 Results

### 4.1 Characterisation

#### 4.1.1 Structural Characterisation

Following the procedure in the method section, a visually homogeneous batch of black-phase perovskite layers was obtained. During the first annealing step the transition from the yellow to the black phase was initiated, while the second annealing step fully transitioned the material into the black perovskite phase. Using the profilometer these samples had a measured thickness of around 350 nm, and the resulting layers are shown in Figure 9. The XRD pattern, shown in Figure 10, shows the distinctive (100) and (200) peaks for

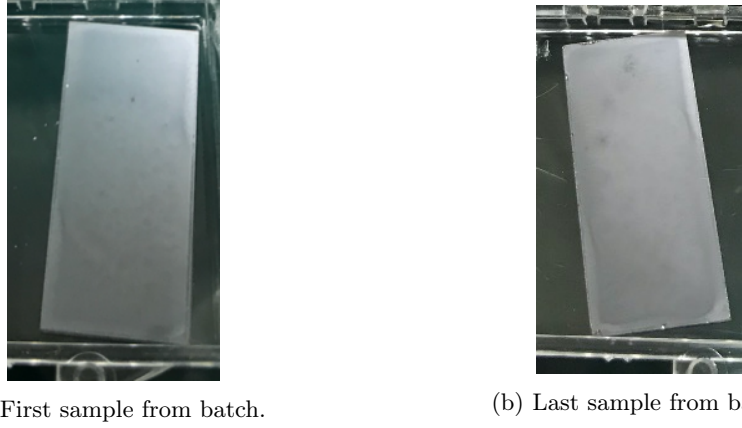


Figure 9: Annealed  $\text{CsPbI}_2\text{Br}$  perovskite thin films, fabricated at the TU Delft.

the cubic perovskite  $\alpha$ -phase at  $17.1^\circ$  and  $34.5^\circ$  respectively, corresponding to the XRD patterns shown in the literature [29]. The small FWHM of the peaks indicates the full

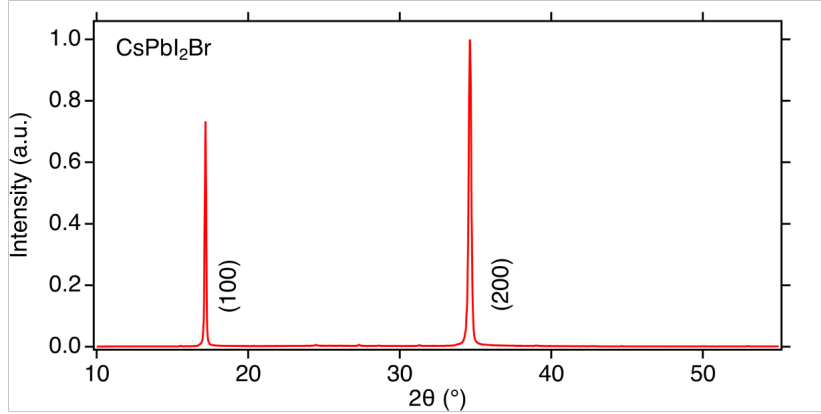


Figure 10: XRD pattern of a  $\text{CsPbI}_2\text{Br}$  perovskite thin films.

transition to the cubic  $\alpha$ -phase since the presence of the perovskite tetragonal phase will lead to broadening of the peak or even peak splitting. From both the appearance and the results of the XRD patterns we can conclude that the structural characterisation indicates that the annealing temperature and duration is sufficient to fully transition the material into the cubic phase without degrading the material.

#### 4.1.2 Optical Characterisation

The fraction of absorbed light  $F_A$  is shown in Figure 11. The onset of the steep absorption shoulder is around 650 nm, which corresponds with the bandgap value of around 1.9 eV, as reported in the literature [71].



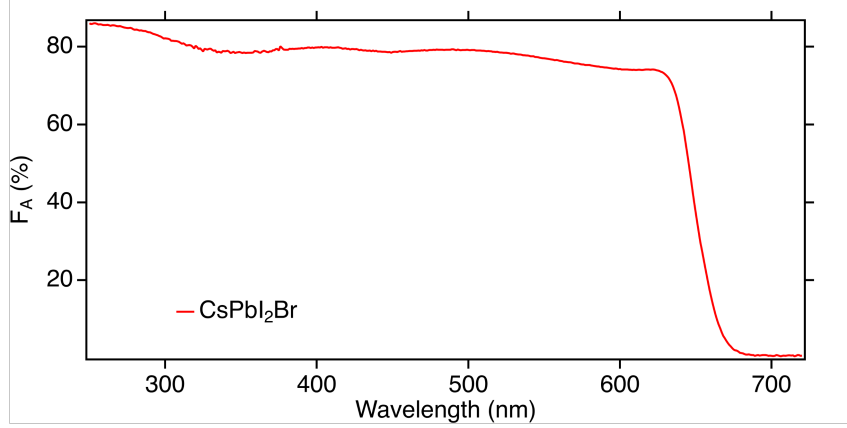


Figure 11: The absorption spectrum in terms of the fraction of absorbed light of CsPbI<sub>2</sub>Br perovskite thin film.

Together with the sharp peaks in the XRD pattern of Figure 10, the steep absorption shown in Figure 11 suggests a full transition to the cubic  $\alpha$ -phase with a well-mixed halide distribution. As discussed in the method section a high illumination intensity can undo this mixing and create iodide-rich regions. This effect was investigated by measuring the PL emission of the perovskite material after an increasing period of illumination and the result is shown in Figure 12.

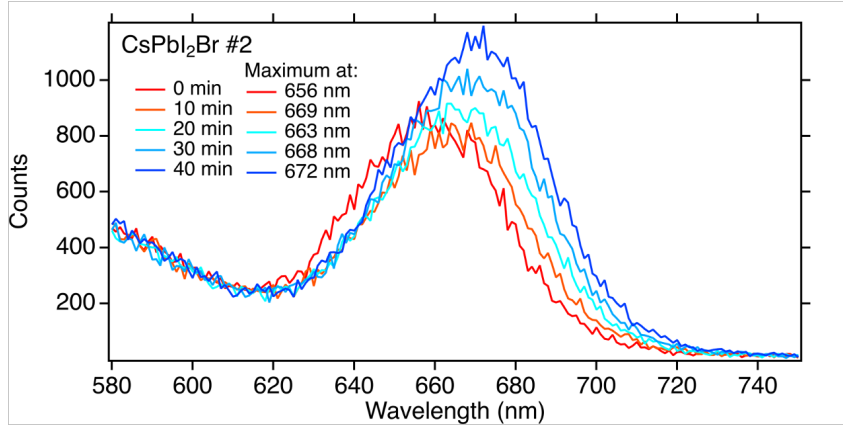


Figure 12: PL emission spectrum after given time intervals of a CsPbI<sub>2</sub>Br perovskite thin film.

The redshift of the PL emission peak at longer periods of illumination indicates that the process of light-induced phase segregation is taking place. The increasing intensity of the PL emission further confirms these iodide-rich regions acting as charge-carrier sinks. It must be noted however that the redshift is minor, compared to mixed-halide perovskite materials with a higher bromide ratio, where a distinctive double peak appears that can be assigned to the bromide- and iodide-rich regions. This was confirmed by measurements done on a CsPbIBr<sub>2</sub> thin film layer that was made during this thesis project and from the literature [72]. The shoulder on the high energy side of the spectrum is caused by the scattering of the illumination pulse by the metal holder, which is not filtered out by the 550 nm long-pass filter. It is worth mentioning as well that the illumination intensity is high, at  $I_0 = 1.2 \times 10^{12}$  photons/cm<sup>2</sup> with a 1 MHz repetition rate. In any case, for the TRMC measurements, the possibility of light-induced phase segregation must be accounted for. Further characterisation of the material was performed by measuring the intensity and wavelength position of the maximum PL emission peak at low temperatures as shown in Figure 13.

The spectra in Figure 13 confirm that the all-inorganic mixed-halide perovskite film follows

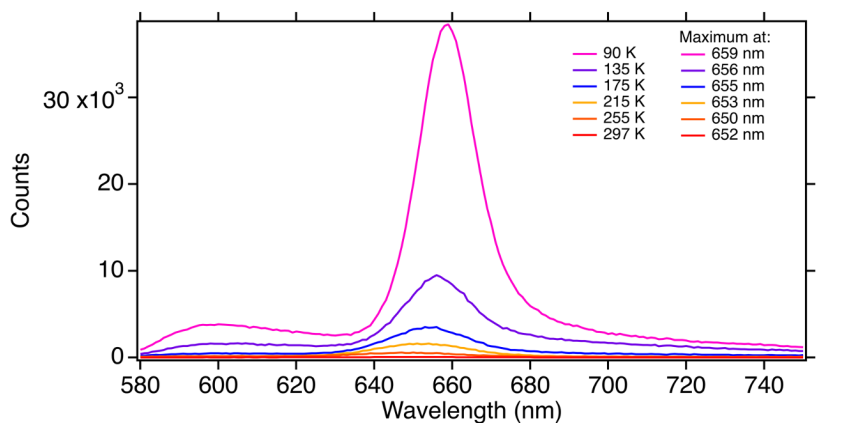


Figure 13: PL emission counts at low temperatures with at the maximum emission wavelength of a CsPbI<sub>2</sub>Br perovskite thin film.

the same trend as lead halide perovskite films in general, namely a thermally activated blueshift and a thermally reduced intensity of the PL emission peak. The increasing intensity for lower temperatures could suggest that less energy is available to break the exciton bonds, with a binding energy of  $E_B = 22$  meV, which would have consequences for the interpretation of the TRMC results, as we will see in Section 4.2. For the current kinetic model that is used for the analysis of the TRMC measurements, it is assumed that there is enough thermal energy available to break the exciton bonds, thus having a unity yield. Other explanations were discussed in Section 2.3.1. The normalised TRPL traces at low temperatures are shown in Figure 14.

The enhanced PL intensity at lower temperatures increases the radiative recombination processes during the initial decay of the TRPL transients. What is especially visible in Figure 14b is that the decay tails become less steep for lower temperatures, indicating a thermally activated decay. As discussed in Section 2.3.1, this indicates that the current illumination intensity regime generates charge-carrier dynamics that are dominated by trap-assisted recombination, since this is a thermally activated process. Since the TRMC measurements will cover illumination intensities that spread both the trap-assisted recombination as the direct recombination dominated regimes and since the intensity of the PL setup induces light-induced phase segregation in the sample, the phase-stability under the illumination of the TRMC setup is something to consider. Before looking at the TRMC results, we will discuss the characterisation of the PSC device that was fabricated using the all-inorganic mixed-halide perovskite layer.

#### 4.1.3 Device Characterisation

For the initial characterisation of the PSC device, which was discussed in Section 2.2, the current-voltage characteristics both in dark and under 1 sun illumination were obtained at room temperature, shown in Figure 15.

The dark JV-curve in Figure 15a shows diode like behaviour, where the charge carriers are injected into the circuit formed by the device exponentially. The current-voltage characteristics under illumination shown in Figure 15b show that the light JV-curve is not simply a shifted dark JV-curve towards a negative current, since the shape isn't kept intact. The S-shaped JV-curve can have different causes, but the charge-selectivity of the transport layers is often appointed as the culprit [73]. Due to interfacial issues, charges might accumulate on either transport layer interface and such an accumulation of charges can increase the recombination at that location [74, 75]. Another cause might be too thin of a layer, which can lead to shunts in the material, but since the measured thickness and corresponding absorption spectrum both confirm a sufficiently thick layer, this influence can be ruled out. However, the existence of an extraction barrier at the transport layer interfaces might have an influence on the assumptions made for the DLTS analysis, such as the capacitance in the

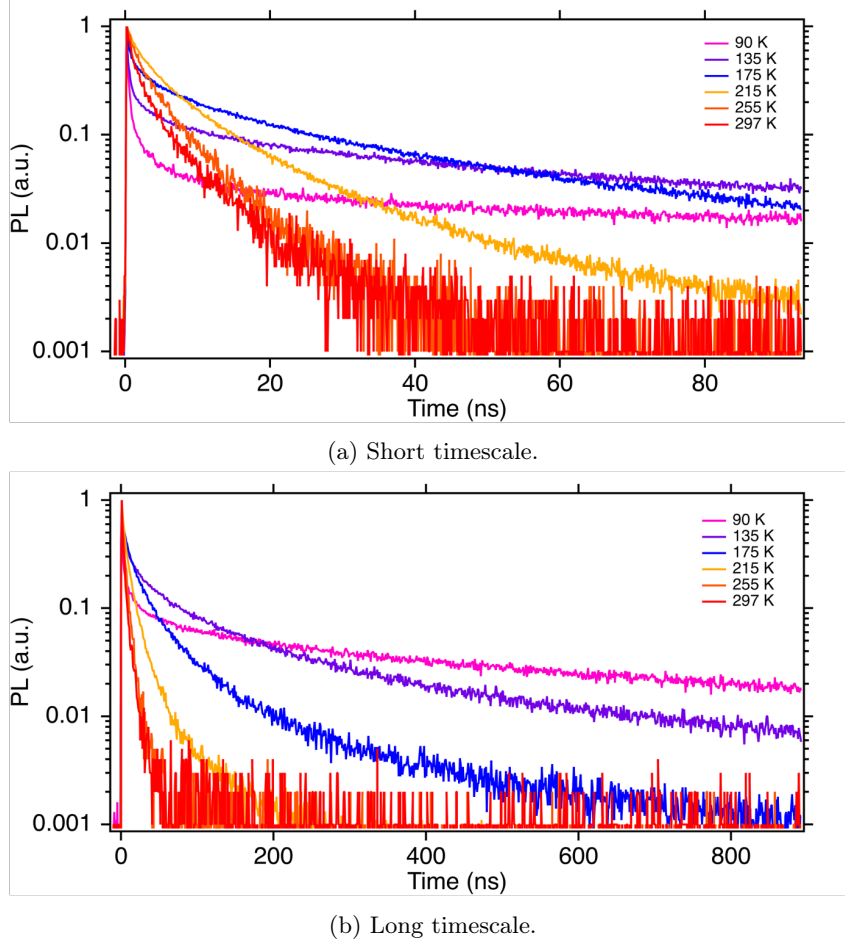


Figure 14: TRPL spectra recorded at low temperatures and shown for two different timescales of a CsPbI<sub>2</sub>Br perovskite thin film.

PSC device only originating from the depletion layer inside the photoactive material. The latter might not be the case if charges accumulate on multiple locations inside the device, thus this must be considered when analysing the DLTS results since this assumes that the depletion layer is only formed around a single p-n junction.

Further characterisation of the device is performed by doing thermal admittance spectroscopy (TAS) measurements at low temperatures, the results of which are shown in Figures 16 and 17. At the low-frequency side of Figure 16 we observe a thermally-activated capacitance peak that originates from the increasing ionic conductivity, as is often observed for halide perovskites [76]. At the very high-frequency domain, we would expect a drop in the capacitance, due to the freezing of the carriers at such a fast-oscillating AC voltage bias, but instead, we observe gradually rising spikes [77]. Since these are observed for all samples that were produced and due to the fact that these spikes do not show for capacitance-frequency measurements done using a different setup, we can conclude that these spikes are setup-related and do not have to be accounted for with physical processes in the material. Since we only measure at a certain frequency, these spikes are expected not to affect the DLTS measurements. To determine which frequency is to be used, the phase delay vs. frequency results are shown in Figure 17. To exclude the influence of the series resistance in the ECM used for the measurements, the phase delay between the current response and the applied voltage must be around  $-90^\circ$ . As is visible in Figure 17, this is the case at 10 kHz, thus this is the frequency of choice for the AC probing voltage bias. Another indication that the spikes appearing in Figure 16 will not affect the DLTS measurements, is that the phase is stable around the probing frequency for each temperature. Before looking into the results of the DLTS measurements, we will view the results and interpretation of the low-temperature TRMC measurements.

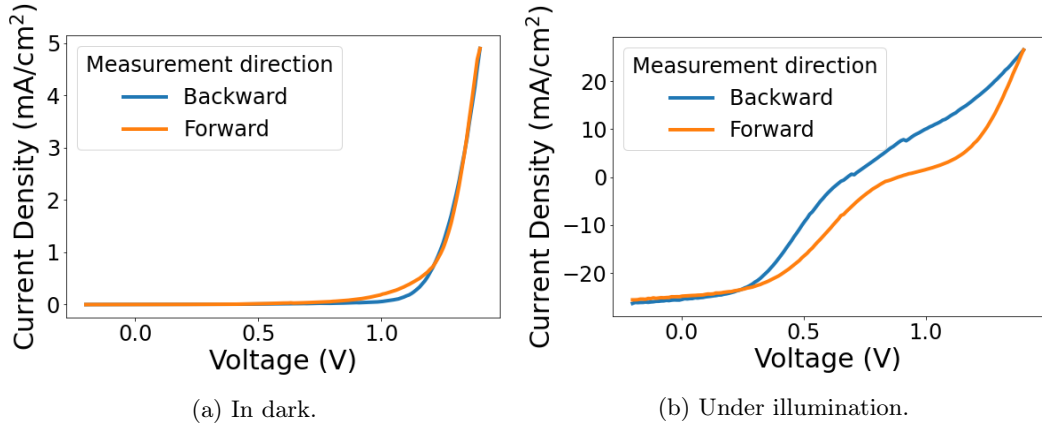


Figure 15: Current-voltage measurements done ranging from -0.2 V to 1.4 V applied voltage bias.

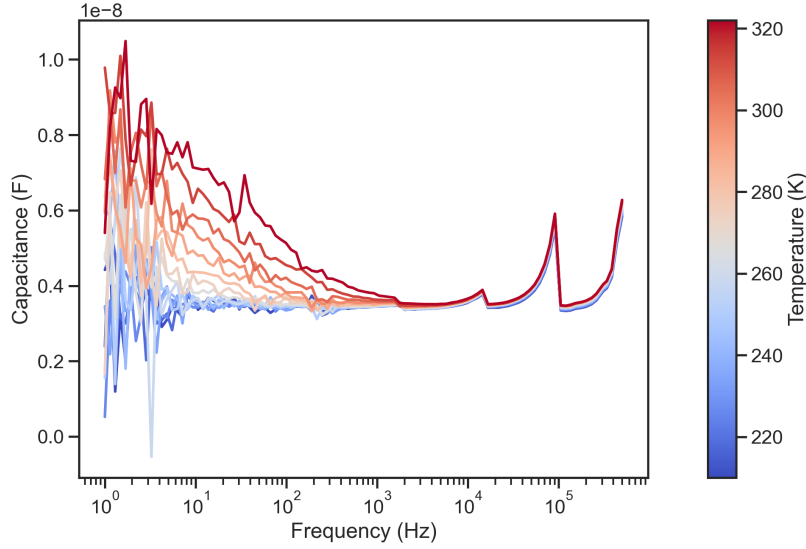


Figure 16: Thermal admittance spectroscopy measurements plotted for capacitance vs. frequency.

## 4.2 TRMC

The TRMC traces were measured of a  $\text{CsPbI}_2\text{Br}$  sample at varying temperatures from 90 K to RT in 8 temperature steps. The resulting traces from the setup using a cavity cell were fitted using the kinetic model described in Section 2.4. Of the 50k iterations per temperature fitting, the final extracted parameters were averaged over the 50 iterations which yielded the lowest residual value compared to the actual measurement. The average of these parameters was fed into the ODEs that govern the kinetic model and the resulting traces are plotted together with the measured traces. The plots will be shown and discussed qualitatively going from the lowest to the highest temperature, where on the left in the figures the full measurement is shown and on the right, the figure is zoomed in on the first microsecond. In this section the traces and fits for 90 K, 200 K and 297 K are shown, the plots for the remaining temperatures can be found in the appendix in Figures 35, 36, 37, 38 and 39.

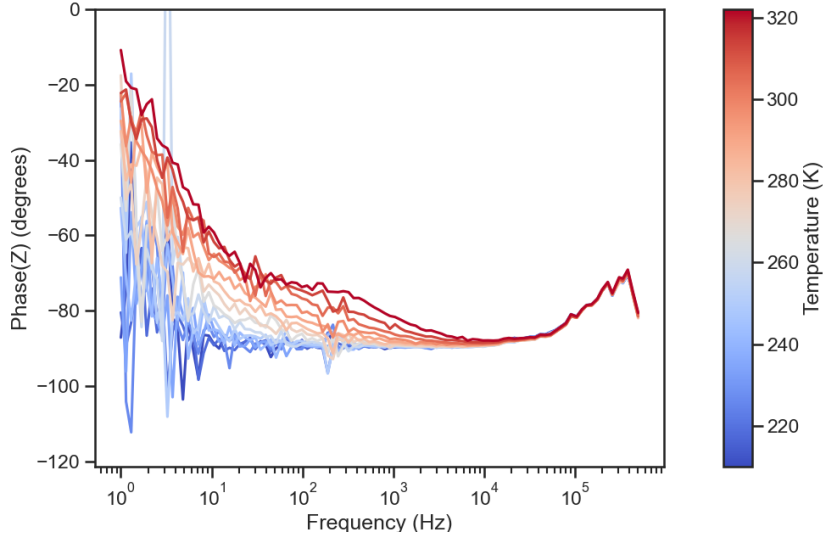


Figure 17: Thermal admittance spectroscopy measurements plotted for current-response phase delay vs. frequency.

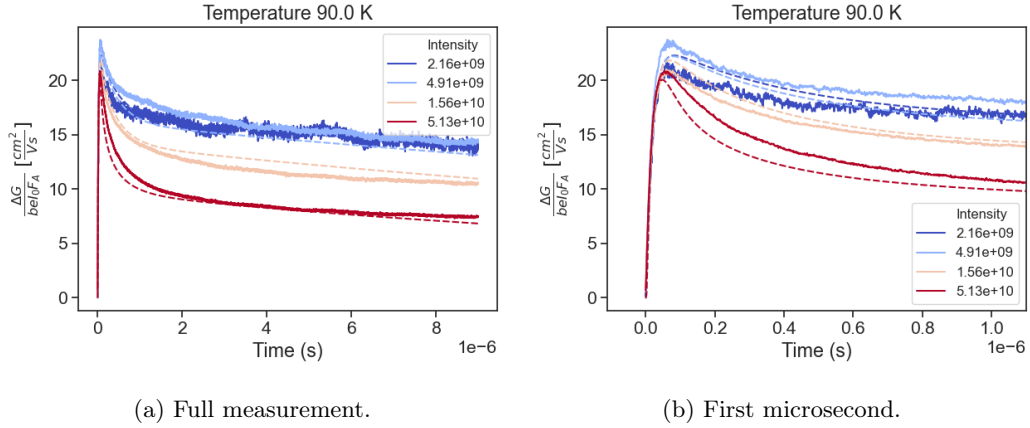


Figure 18: Measured and fitted TRMC traces at 90 K.

### Qualitative Results

Before looking at the extracted parameters, we will qualitatively discuss the resulting traces and the fits. The first thing that stands out is the decrease of the intensity of the normalised change in conductance signal for increasing temperature, with a maximum value of around  $\frac{\Delta G}{\beta e I_0 F_A} \approx 24 \text{ cm}^2(\text{V.s})^{-1}$  for the 90 K traces in Figure 18 which decreases to  $\frac{\Delta G}{\beta e I_0 F_A} \approx 6 \text{ cm}^2(\text{V.s})^{-1}$  for the RT measurements shown in Figure 20. This behaviour is consistent with a mobility that is limited by acoustic phonon scattering as discussed in Section 2.3.1.

In terms of the decay, it is clear that the recombination of the free charges is thermally activated, with the flattening of the decay slopes at lower temperatures in Figures 18 and 19. This indicates a larger fraction of the free charges being trapped in electronic defects from which the trapped electrons can either recombine non-radiatively with the free holes in the valence band or be emitted back to the conduction band. Both these rates are slower than the direct recombination, thus the slopes become more even. The higher intensity of the tails means that more free charges contribute to the signal, in particular, the remaining concentration of free holes that have yet to recombine with the electrons, which are partially trapped. This thermally activated decay matches with the decay observed for the TRPL measurements in Figure 14, where the long tails suggest trap-assisted non-radiative recombination dominated regime. However, there is a discrepancy here since the illumina-

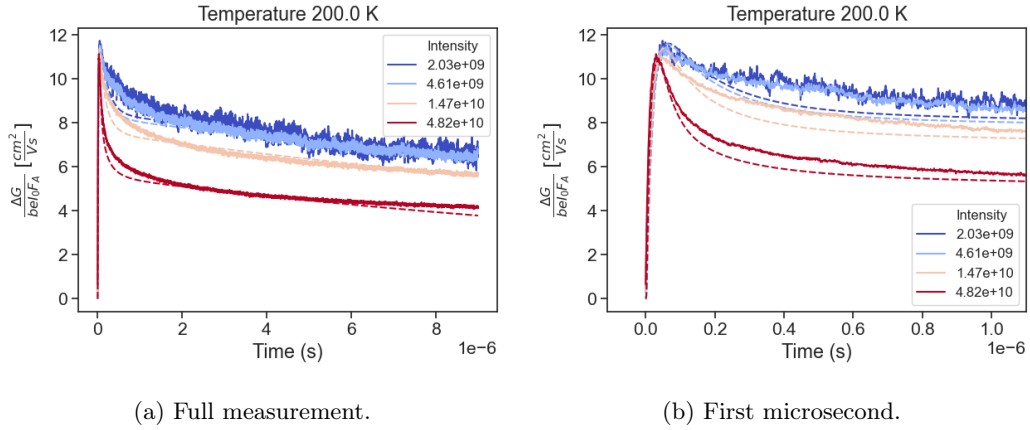


Figure 19: Measured and fitted TRMC traces at 200 K.

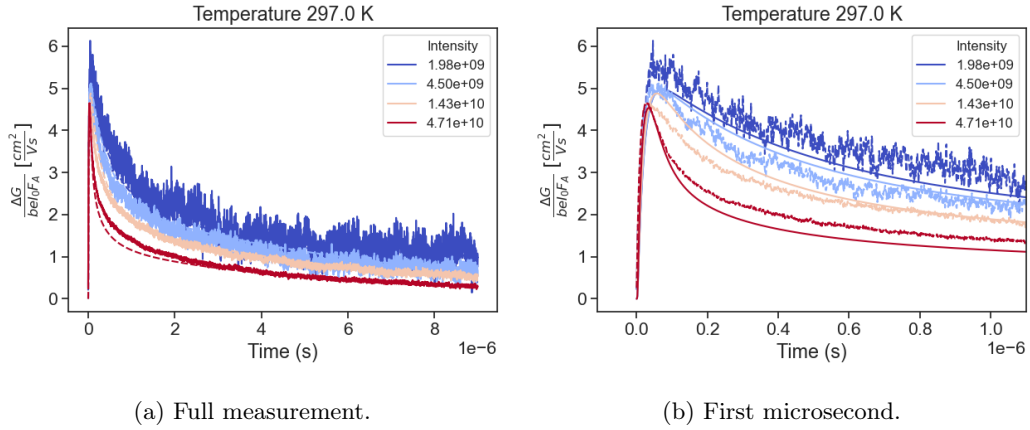


Figure 20: Measured and fitted TRMC traces at 297 K.

tion intensities for the TRMC measurements using the cavity cell have a maximum value of around  $I_0 \approx 5 \times 10^{10}$  photons/cm<sup>2</sup> per pulse, while the TRPL is measured using an excitation source with a  $I_0 \approx 10^{12}$  photons/cm<sup>2</sup> per pulse intensity. As can be seen from the open cell data from the TRMC in Figure 40 in the Appendix, the higher illumination intensities clearly show a direct-recombination dominated domain, indicating that the concentration of photo-generated charge-carriers exceeds the concentration of electronic traps, while the maximum illumination intensity is in the same order of magnitude as the one used for the TRPL measurement. A possible explanation for this might lay in the difference in the illumination surface between both methods. The TRMC illumination covers the whole sample, thus generating charge all over the material and in the case of a high illumination intensity, all available trap states will be saturated, leading to a direct-recombination dominated regime. During the TRPL measurements, the sample is illuminated with a much more narrow laser pulse. The area covered by this pulse might not cover a whole grain in the polycrystalline material. Due to the local nature of the charge generation, not all trap states in the grains of interest might be saturated. Locally this saturation might occur, but the free charge carriers can diffuse easily to the surroundings, where plenty of unfilled trap-states are present, either in the grain itself or on the GBs. This may lead to the measured thermally activated decay in the TRPL measurements, despite the illumination intensity being in the same order as the highest intensity used for the open cell TRMC measurements. Figure 40 in the Appendix sum up the qualitative conclusions for the TRMC measurements, namely that the decay of free charge carriers becomes increasingly direct-recombination dominated for increasing temperature as well as increasing illumination intensity.

### Light-stability

As the illumination intensities of the TRMC measurements approach that of the laser intensity from the (TR)PL setup, a careful inspection of the phase stability under illumination must be performed, since the results shown in Figure 12 clearly indicate light-induced phase segregation under the illumination of the sample. For this, it was attempted to measure the PL spectrum of the sample in-situ in the TRMC setup, but we were currently unable to extract a measurable PL signal in this manner. However, we could measure the effect of the light-induced phase segregation indirectly by comparing the charge-carrier lifetime at the same temperature, before and after the full measurement cycle, the results of which are shown in Figure 21. If the illumination pulses would cause a significant amount of iodide-rich

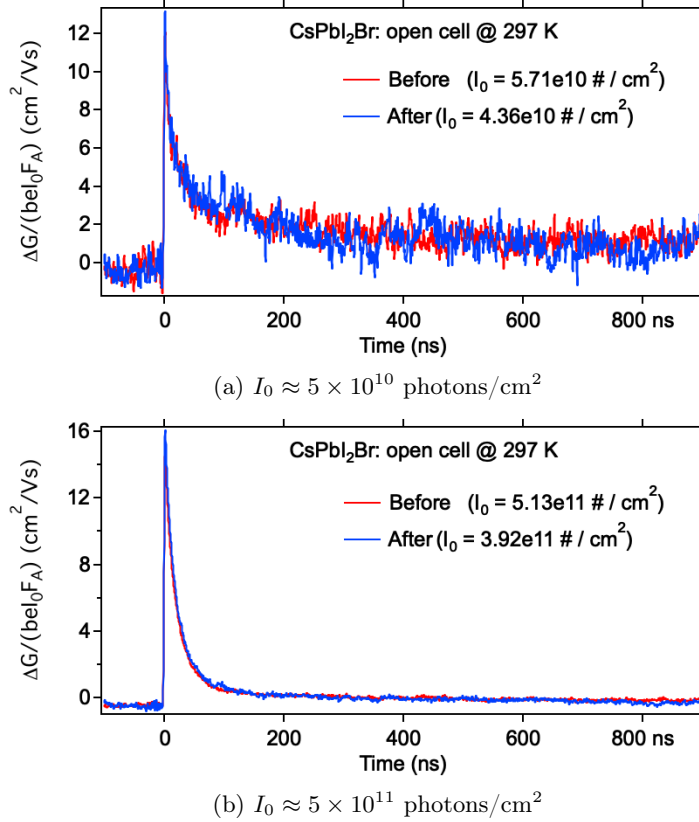


Figure 21: Overlapping TRMC traces measured at 297 K before and after low temperature measuring cycle.

region, an expected decrease in the charge-carrier lifetime should be visible, since these regions act as charge-carrier sinks which mediate faster direct recombination. Since the TRMC traces in both Figure 21a and 21b overlap completely, we can conclude that the material is sufficiently stable under the TRMC illumination. This indicates that either light-induced phase segregation occurs only slightly or not at all. In the case of the PL measurement, the redshift of the PL emission peak was about  $\sim 16$  nm, which is already minor compared to the double PL emission peak appearing for all-inorganic mixed-halide perovskite samples with a higher bromide ratio, thus the effect of this on the lifetime of charge-carriers can be expected to be limited. Together with this result the sheer amount of pulses during the 40 minutes illumination period of the PL emission measurements far exceeds the number of pulses that hit the sample during a full day of TRMC measurements. The repetition rate for the PL measurements is 1 MHz, which results in  $2.4 \times 10^9$  pulses during the PL measurement. Before reaching this amount of pulses using the TRMC setup, one has to measure the sample continuously for over 7.5 years. It can thus be concluded that despite the same intensity per pulse, the overall illumination intensity for the PL setup has a far greater effect on the phase stability than the TRMC setup.



## Mobility

With the light stability during the TRMC measurements being confirmed, we will now turn to the extracted parameters of the fits using the proposed kinetic model. Figures 22 and 23 show the global governing parameter results of the fits for varying temperatures, while in the Appendix Figures 41 and 42 show the parameters linked to the deep and shallow trap respectively. The full table with the extracted parameters can be found in the Appendix in Table 1.

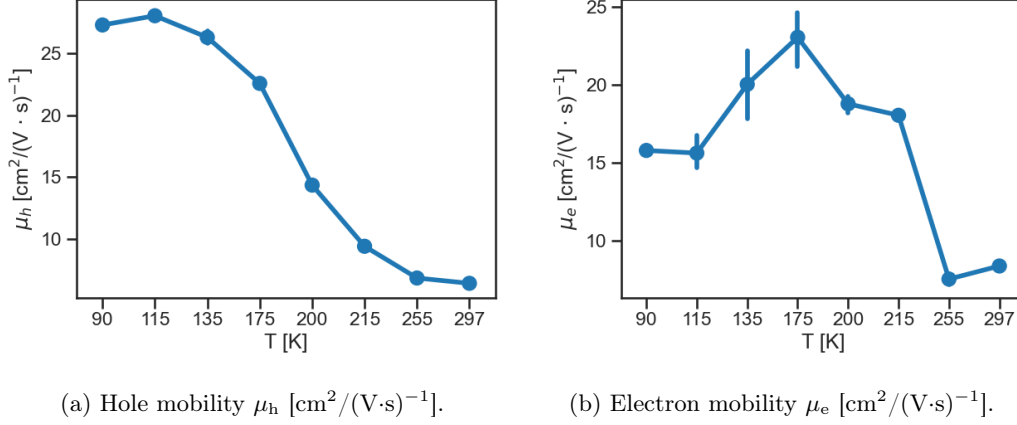


Figure 22: Mobility parameter values plotted for varying temperatures.

The first set of parameters drawn from the TRMC fits are the respective hole and electron mobility values, shown in Figures 22a and 22b. Since the measured traces were obtained using a cavity cell, the excitation intensity is in the lower half of the TRMC excitation intensity range. This results in the decay kinetics being dominated by trap-assisted recombination, as we have mentioned in the section above. Since a significant amount of majority carriers end up being trapped, the remaining holes are contributing the most to the TRMC signal. The sum of the mobilities that give rise to the signal intensity is mainly determined by the hole mobility value in this domain. This shows in the smooth curve for  $\mu_h$ , while  $\mu_e$  is less well-determined and has large error margins. Especially  $\mu_h$  shows the increasing mobility value for lower temperatures, which is as expected. However, this increase stagnates and flattens out below 175 K, which can have several reasons either fitting related or physical of nature. In terms of the fitting process, the set parameter boundaries might be too restrictive for the lower temperature hole mobility values. The boundaries are not shown, since these were changed for each temperature accordingly to guide the fitting algorithm towards solutions that made physical sense. If for example the hole mobility was allowed to go high, it would look in that direction and compensate by setting the lowest possible electron mobility value that was allowed by the set parameter boundaries. The resulting ratio between the mobility values of the two charge carriers that could exceed one order of magnitude was nonphysical and thus the mobility boundaries were set such that the fitting algorithm would assign similar values to both charge carriers. However, the upper limit of the hole mobility at 30 cm<sup>2</sup>/(V·s)<sup>-1</sup> for the lowest three temperatures might be the reason that the extracted value from the fits stabilises just below that value. However, one can argue that the mobility would have to stabilise at these temperatures since the intensity of the measured TRMC traces at these temperatures stabilises as well. Thus, the flattening out of the hole mobility value might have a physical reason. One explanation was already mentioned, namely that the perovskite experiences a phase transition from the cubic to the tetragonal phase below these temperatures. However, to fully transition the material back into the cubic phase, one would need to anneal the material to a sufficiently high temperature. During the sample preparation for this thesis, the minimum temperature required to get rid of the XRD peak splitting, which indicates the presence of the tetragonal phase, was found to be 160 °C. When heating the sample back up to RT, the TRMC traces however show that the decay kinetics and mobility values are identical as prior to the cooling down process, which tells that the material is in the same structural phase, making the phase transition at lower tem-



peratures unlikely. Another explanation might lay in the reduction of thermal energy in the material to break up the excitons into free charge carriers. This argument was already given for a possible explanation of the increased PL intensity at lower temperatures, but it can also give rise to the reduction in the apparent charge-carrier mobility values. In the kinetic model the yield is defined which tells what fraction of absorbed photons creates free charge carriers and this value is currently set to unity for the entire temperature range. Around RT this assumption is valid since the excitons have a relatively low binding energy of  $E_B = 22$  meV, but at 90 K when the present thermal energy is around  $E_t = 11.6$  meV, this may not hold anymore. The result of using the unity-valued yield is that the model assumes that there are more free charge carriers contributing to the change in conductance signal than there are actually free charge carriers present in the physical material. This will lead to the model assigning a lower mobility value to each charge carrier, while in fact, this mobility value of each individual charge carrier might still increase for lower temperatures. Methods to confirm either of these theories will be discussed in Section 6.

### Fitting parameters

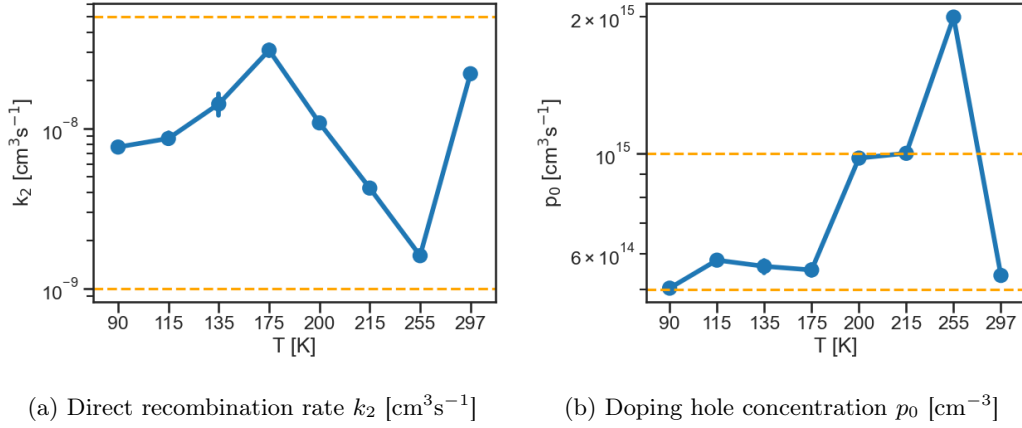


Figure 23: Global fit parameter values plotted for varying temperatures, with the parameter boundaries given by the orange horizontal lines.

The plots for the direct recombination rate  $k_2$  and the excess hole concentration  $p_0$  are less easy to interpret. Starting for Figure 23a the value of the direct recombination increases from 90 K to 175 K, which is as expected from the reduced lifetime at higher temperatures in the measured traces of Figures 18 and 19. However, the value nears the set boundary limit, shown by the orange line in Figure 23a, for the fitting process at around 200 K and thus it is suggested that for 200 K the fitting algorithm searches for a suitable fit by compensating the other parameters. This leads to a reduction of the direct recombination rate, all the way down to the lower limit being reached at 255 K, after which the fit parameter value spikes up when going to RT. The latter order of magnitude increase in 42 K is nonphysical and can again only be assigned to the too restrictive fitting parameter boundaries. Since the direct recombination terms in Equations (11) and (12) are additionally determined by the concentration of excess holes  $p_0$  and since the measured direct recombination rate steadily increases for higher temperatures, the strong reduction in  $k_2$  is compensated for by an increase in  $p_0$ . Only at RT, when  $k_2$  reaches its lower limit, and  $p_0$  has reached its upper limit, they both change abruptly in the other direction. In Figure 23b the value of  $p_0$  exceeds the set boundaries at 255 K, since here the boundary value was accidentally set to  $p_{0,\max} = 2 \cdot 10^{15}$  cm⁻³, but this only confirms the assumption that the fitting algorithm is restricted by the upper boundaries since it will go in that direction if it is allowed to do so. For the remainder of the fitted parameter values, the fitting parameter boundary values remain too restrictive. This breaks trends in the thermal activation for the rates governing the deep and shallow trap in a similar fashion as for the direct recombination rate, where the other parameters compensate for the hit limit, which draws the rate in a different direction. Only partial temperature-dependent trends are visible, such as in Figure 24, where both

for the lowest and highest three consecutive temperatures the expected thermally activated trend becomes visible, only to be disrupted by the confining parameter boundaries, shown in Figure 24a for the deep trap. Since the rates for the shallow trap are defined as a ratio of the value found for the deep trap, the boundaries change for each separate deep-trap value and thus for each temperature. This is why the boundaries are not plotted for the rates of the shallow trap. The complete overview of the trap parameter temperature dependence can be found in the Appendix in Figures 41 and 42. In Figure 42c the value exceeds the set boundary at the lowest temperature, but here the similar argument holds as for the excess hole concentration, shown in Figure 23b.

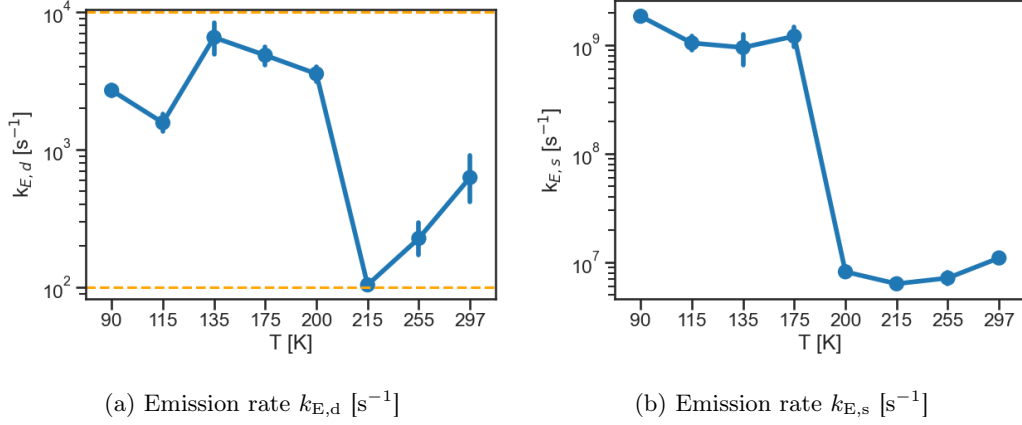


Figure 24: Deep trap fit parameter values plotted for varying temperatures.

### Expanded parameter boundaries

First attempts at expanding the parameter boundaries were made, where the average was taken over a set of iterations similarly to the fits shown earlier in this section. To investigate the existence of multiple local minima, for 200 K the averages were taken of 4 independent sets of iterations to check if the system would find the same parameter value after each complete run. The full table with all the extracted parameters for the wide parameter boundaries can be found in Table 2. The results for the mobility values are shown in Figure 25.

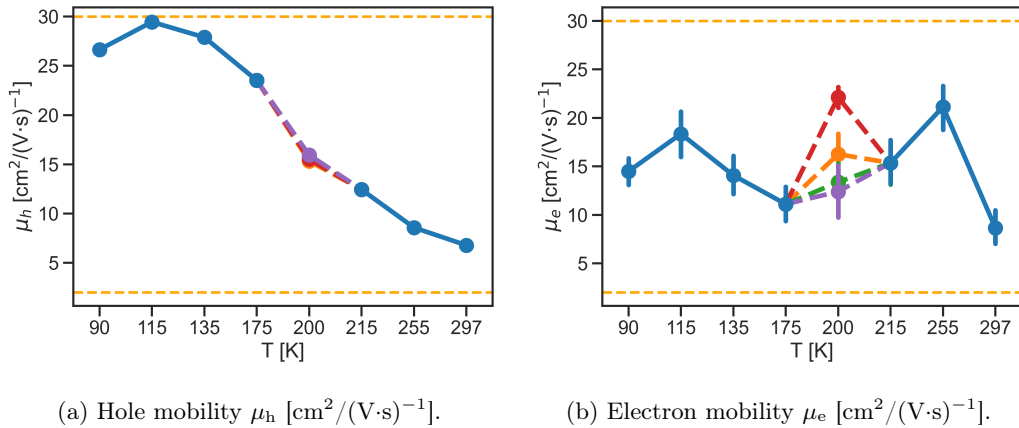


Figure 25: Mobility parameter values plotted for varying temperatures using a wide parameter boundary range.

The values for the parameter boundaries of the mobility values were not extended compared to the original fitting method, since the value of the mobilities is strongly linked to the value of the TRMC signal. If one would for example set the parameter boundary range for the hole mobility higher than 30 cm<sup>2</sup>/(V·s)<sup>-1</sup>, it would only find a suitable fit if the

electron mobility would be brought down towards the lower limit. If this lower bound was not given, then the electron mobility value was seen to drop to negative values in order to compensate for the high hole mobility value. Since this is nonphysical, the hole mobility values were constrained to be at most  $30 \text{ cm}^2/(\text{V}\cdot\text{s})^{-1}$ . Still, just as for the set parameter boundaries for the original fitting, these might be too restrictive at lower temperatures for the hole mobility values, which might lead to the trend breaking visible in Figures 22a and 25a. What is interesting to see in Figure 25a is that the deviation of the hole mobility value at 200 K is minor for each of the different runs, while for the electron mobility the values vary significantly. This has to do with the strong dependency of the signal amplitude of the calculated TRMC fits on the hole mobility value, leaving not much room for different values, while at the same time the system is insensitive to the electron mobility value. Similarly, as explained for the earlier found mobility values, this is due to the measured traces being in the trap-assisted recombination dominated regime, such that the majority of the electrons get trapped rapidly, leaving the remaining holes to contribute the most to the signal.

As Figure 26 shows, for some parameter values the newly set boundaries suffice in letting the fitting algorithm look for different values without clipping or breaking the trend, such as for the excess hole concentration  $p_0$  shown in Figure 26b, but since the direct recombination rate  $k_2$  among others is reaching one of the boundaries, as shown in Figure 26a, the resulting values of the other parameters will ultimately be compensating for the saturation of this particular parameter value. It must be noted, however, that the multiple values for  $p_0$  at 200 K all follow the visible trend, thus indicating that the system is sensitive to the concentration of excess holes and that it finds similar values for multiple fits.

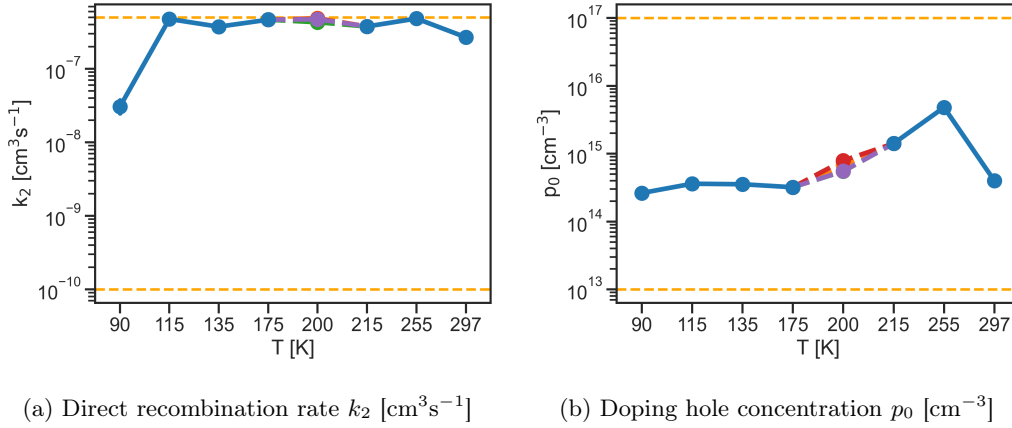


Figure 26: Global fit parameter values plotted for varying temperature for a wide parameter boundary range, with the parameter boundaries given by the orange horizontal lines.

To complete the analysis of the fits using wide parameter boundaries, the emission rates are plotted in Figure 27.

The desired effect was to allow for the exponential growth of the emission rates using wide parameter boundaries, which is expected physically, but this does not show for both the emission rates for the deep and shallow traps respectively. This can have multiple reasons, but the parameter boundaries being still too restrictive for some parameters might be one of them. Additionally, the values at 200 K vary significantly, indicating that the system is trying to fit the data using multiple paths. The remainder of the fitting parameter values using the wide parameter boundaries can be found in the Appendix in Figures 43 and 44.

In the Discussion and Outlook, the limitations of the currently applied parameter boundaries will be discussed in-depth and several options will be discussed on how to expand these boundaries even further to obtain fits of the measured traces, where the focus must be on the physical assumptions for the temperature-dependence of these parameters.

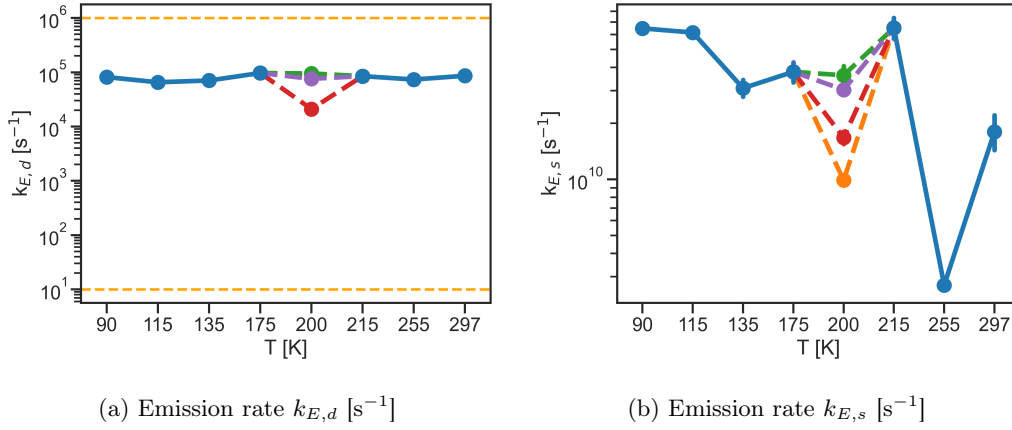


Figure 27: Deep trap fit parameter values plotted for varying temperatures using wide parameter boundaries.

### 4.3 DLTS

In this section, two sets of measured traces are shown and discussed for each device pixel, where one can be labelled as a DLTS measurement and one as a TID measurement. The distinction between the two lies in the filling pulse width and the reason why both are shown in the DLTS results section is motivated as follows. In Section 3.4 about the methodology for the DLTS measurements, it was mentioned that a filling pulse width of 10 microseconds was used to obtain the capacitance transients. In the field of DLTS measurements, the usual filling pulse lengths can be two orders of magnitude smaller, but for these short pulses no capacitance transient was recorded, thus the lowest value that gave rise to a signal was used. As explained earlier, the idea for DLTS is to keep the filling pulse as small as possible to avoid the interference of ion movement on the change in capacitance. The latter dynamics are usually captured by using filling pulses in the order of seconds, but in some cases, TID measurements are performed with filling pulses as small as 10 milliseconds. To determine the origin that gives rise to the capacitance transient for the short filling pulse used in this thesis, both the results of the short and long filling pulses are shown and analysed.

#### Qualitative results

To start off, the capacitance transients for a given device pixel are shown in Figure 28 for the different filling pulse widths.

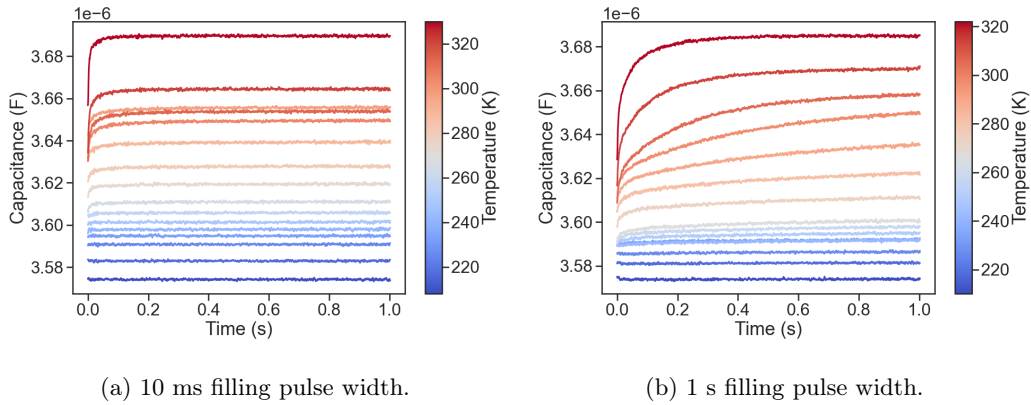


Figure 28: Capacitance transients for the first analysed pixel of the first device (D1P1) using two different filling pulse widths.

Qualitatively we observe a thermally activated rise in capacitance for both figures, where Figure 28a shows a faster rise than Figure 28b. This capacitance transient becomes visible

for temperatures exceeding 255 K, so in the analysis of these measurements, the temperature steps below 255 K are neglected.

#### 4.3.1 Fitting parameters

Using Equation (20) these traces were fitted and the resulting extracted  $c_i$  parameter values and activation energies for both the short and long filling pulses are shown in Figures 29 and 30, with the full table of extracted parameter values located in Table 3 in the Appendix.

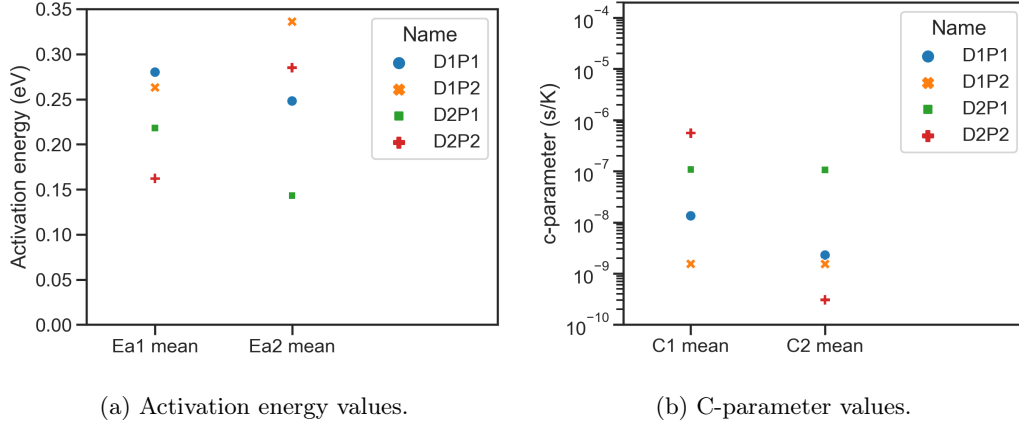


Figure 29: Extracted parameter values from the best fits of the capacitance transients observed with a filling pulse of 10 ms.

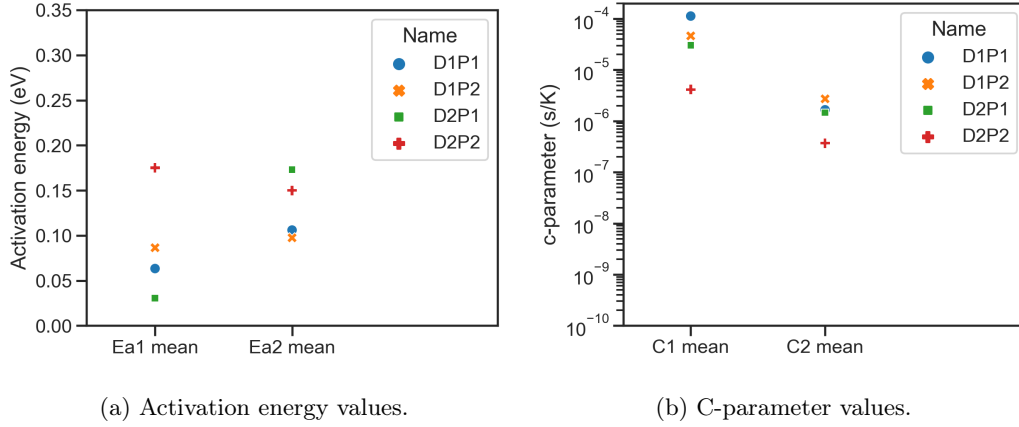


Figure 30: Extracted parameter values from the best fits of the capacitance transients observed with a filling pulse of 1 s.

In Figures 29 and 30 the two devices are denoted by D1 and D2, with P1 and P2 being two different pixels on the respective devices. The resulting activation energies for the short filling pulse measurements range from 143 to 336 meV, shown in Figure 29a, while the activation energies for the longer pulse in Figure 30a range from 30.4 to 175 meV. In general, the trend is that the activation energies of the long filling pulse transients are lower than the ones for the short filling pulse. The first indications are that the two different sets of transients have one overlapping process with an activation energy of around 150 meV. The 10 ms filling pulse further shows a process with higher activation energy  $E_A \geq 220$  eV, while the 1-second filling pulse has a contribution with an activation energy below 100 eV. As expected, the  $c$ -values become higher for slower transients, but what stands out is that the  $c$ -values tend to increase for a lower activation energy, which seemingly correlates the two values. Especially the difference between the two types of measurements is visible, where the 1-second filling pulse measurements show a tendency towards lower activation energies, paired with higher  $c$ -parameter values. As is visible in Figure 28 the 1-second filling pulse

measurements show slower kinetics in the capacitance transients. If we look at Equation (20), a decreased change over time is achieved by an increase in the exponential denominator, or in other words, by an increase in the  $c_i$  value or an increase in  $E_{A,i}$ . Both these parameter values should in this model be able to change independently from one another, however, the trend in the extracted values shows the interdependence of the two.

### Correlation $E_{A,i}$ and $c_i$

This correlation was investigated further by inspecting a scatter plot of pairs of  $c$ -values and activation energies for multiple repetitions, shown in Figure 31.

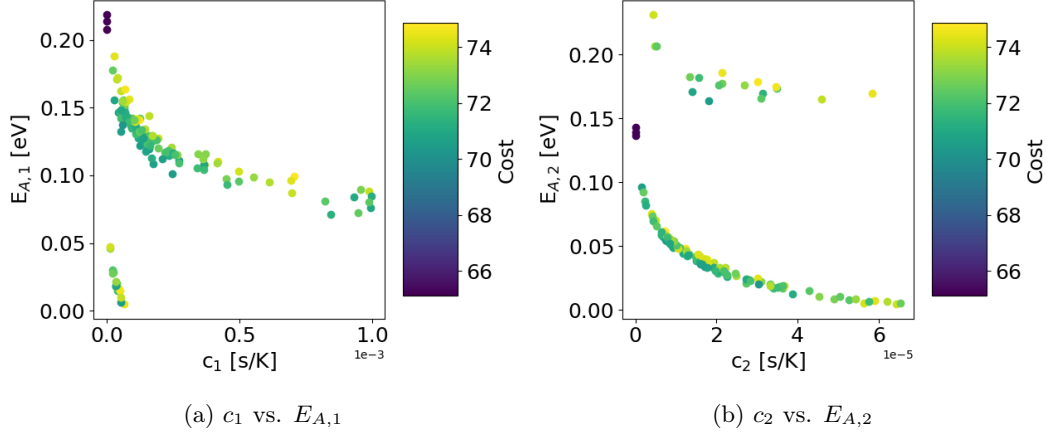


Figure 31: Scatter plots of the  $c$ -parameter values against the activation energies of both exponential contributions for the first pixel of the second device (D2P1). The colourmap indicates the value of the residual between the calculated fits and the actual measurements.

In Figure 31 the quality of the fit is indicated by the colour of the scatter-point, where the darker it gets, the smaller the residual is between the fit and the measurement and thus the better the fit is. For both exponentials, a clear correlation is visible between the activation energy and the  $c$ -parameter. The points included in Figure 31 are however a selection of the entire set of 200 repetitions for this simulation, selected by setting a threshold in the maximum residual value. For these plots, this threshold was defined by multiplying the lowest residual value by 15%. Figure 32 shows the scatter plot of all repetitions values, including the runs that achieve a high residual value by not fully converging to a good fit.

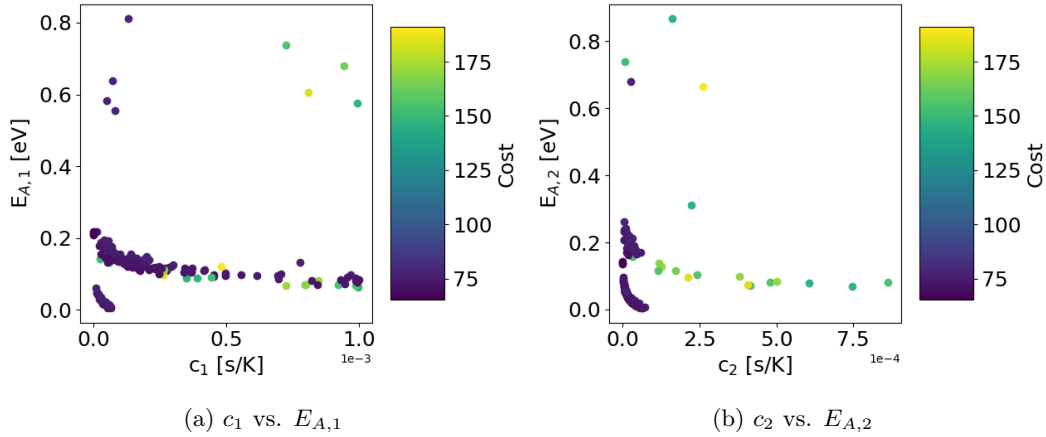


Figure 32: Scatter plots for the full set of repetitions of the  $c$ -parameter values against the activation energies of both exponential contributions for the first pixel of the second device (D2P1).

From Figure 32 it becomes clear that not all combinations of  $c_i$  and  $E_{A,i}$  fall on the same curve. This is an indication that initially, the fitting algorithm considers every possible

combination of these values inside the set boundaries and that these values are thus not fundamentally linked in the model used to describe these transients. This does not provide enough evidence to ensure this, which will be discussed in Section 6. What is, however, clearly visible, is that for each local minimum the fitting algorithm looks for better solutions along a well-defined curve in the  $c_i$  vs.  $E_{A,i}$  space. In the case of Figure 31 there are three local minima visible, which are made visible in the scatter plots between the two activation energies in Figure 33b.

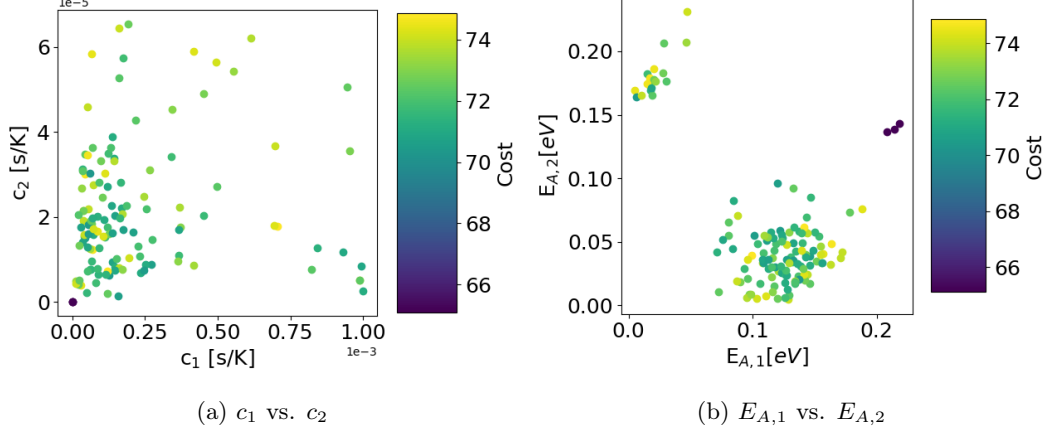


Figure 33: Scatter plots for the extracted parameter values of both exponentials in pixel D2P1.

When the repetition during the fitting process reaches a local minimum, it is clear that it tries varying around the combination of activation energy values, creating a strong link between the two. The corresponding  $c$ -parameters are not that visibly linked together but are scattered all over the given parameter space, but this can be due to the minima appearing only for a log-log plot. One clear link between the two scatter plots exists for the three fits with the lowest residual value, located in Figure 33b on the far right. This combination of high  $E_{A,1}$  and relatively high  $E_{A,2}$  would lead to a fast-rising transient, but for the resulting good fits, these activation energies are compensated by very low  $c_i$ -values, visible in the bottom-left corner of Figure 33a. Just as in Figure 32 compared to Figure 31, the distribution of scatter-point solely located around local minima disappears when plotting the full set of repetitions, which can be seen in Figure 45 in the Appendix.

### Physical origin of capacitance transients

Due to the strong correlation between the  $c$ -values and the activation energies for fits with a low residual value, it is difficult to draw conclusions on the difference in activation energies between the transients measured after the short and long filling pulses. If these were actually different physical processes that caused the transients for the two different pulses, this would have consequences for the fitting approach. In an ideal situation, the short filling pulse would only trigger electronic processes, while the longer filling pulse additionally creates ionic movement. For the longer filling pulse, however, these electronic processes would still occur and be measured together with the additional ionic processes, thus an increasing amount of exponentials would be required to fit the transients properly. What is observed, however, for this set of transients is that adding a third exponent to the long filling pulse measurement fits does not drastically improve the resulting fits, with an improvement in the remaining residuals of only a few per cent at most. If an additional process would occur during the long filling pulse measurement, this additional exponent would be crucial and would lead to a significant betterment in the fit. Another indication of the same processes being at play for both filling pulse widths is that the improvement for adding a third exponent for the long filling pulse measurements in terms of the residual has the same ratio compared to the fit with two exponents for the short filling pulse measurements.

The difference in the activation energies is thus difficult to interpret since the fitting results suggest similar processes occurring for both filling pulse lengths. The activation



energy difference can either have a physical origin or might be the product of the fitting algorithm approach. To start off with the latter the difference in the  $c$ -parameter values is considered. The faster rises of the short filling pulse measurements are coupled with relatively small  $c$ -values, while the slower transients of the longer filling pulse are assigned with  $c$ -values of about three orders of magnitude larger. When considering Equation (20), this is what is expected, since a smaller denominator value in the exponent will lead to a faster change over time, while a larger denominator value will lead to slower transients. However, it might be the case that the fitting algorithm is not able to distinguish the activation energy, which defines the thermal activation of the process, with the  $c$ -parameter value that is primarily governing the rate of the transients. In this sense, the increasing  $c$ -value for longer filling pulses are compensated by a lower value for the activation energies. Increasing the temperature resolution can be a solution for this, as will be discussed in Section 6. A physical explanation for the lowering of the activation energy might be that for longer filling pulses a higher concentration of ions is present deep in the depletion layer. When the forward bias is removed, the ions will not only drift, but it might be possible that a diffusional force will contribute to the ion migration, which could lead to a lower activation energy for the displacement. However, a counter-argument could be given that a higher concentration of mobile ions will result in a reduction in the possible pathways of ion migration, which could increase the activation energy for ion movement.

With certainty can be said that both exponents contribute to a rising transient, which means that the capacitance increases over time consisting of two processes. A rising transient that is caused by an electronic process is the capacitance change due to majority-carrier trap-filling. In the case of a p-type material this means that instead of traps being filled with electrons, the electrons are pushed out of the traps and thus become filled with holes, which is the opposite of what was explained in Section 2.5. In the case of an n-type material, which is suggested by the analysis of TRMC measurements on full-bromide perovskite materials, this would mean that the majority-carrier electrons fill the trap states during the bias pulse [50]. The consequence of the presence of majority carrier traps on the kinetic model applied for the TRMC analysis will be discussed in the next Section 5. In the case of ionic drift, the rising transient could be explained for both the p-type as well as the n-type assumption. In the case of p-type material, the rising transient means that the ionic movement causes the depletion region width to decrease, which can be attributed to cations moving towards the p-n junction. Since the material consists of two cation types, both caesium and the heavier lead-ion in the perovskite material can contribute to this ion drift. If however, the material has an n-type nature, then anions are giving rise to the capacitance transient when moving towards the interface. Since this is a mixed-halide material, both bromide and iodide ions can contribute to the signal, each with their own respective ionic dynamics.

If indeed the capacitance transients are caused by ion drift, the difference in the rate of the rise between the short and long filling pulse must be explained. A possible explanation might be that for a short filling pulse ions are moved over a limited distance. When the bias pulse is removed, the drift of ions will happen relatively swiftly back to the equilibrium conditions. However, when a longer bias pulse is applied, the distance over which the ions move will increase significantly and since ions are relatively slow compared to electronic charges, the drift over an increased distance will give rise to a longer transient.

In the next section we will discuss and compare the results from the TRMC and DLTS measurements.



## 5 Discussion

By combining the results from both the TRMC and the DLTS measurements, the primary goal of this thesis was to shine a light on the temperature dependence of the electronic charge-carrier dynamics in all-inorganic mixed-halide perovskites and the effect of electronic trap states on these dynamics. Both methods have a fundamentally different working principle, but one of the material properties that can be extracted from either method is the thermal emission rate for trapped charge carriers. By creating an Arrhenius plot, the extracted emission rates for both traps in the kinetic model used for the TRMC measurements can be compared with the activation energies of the fitted DLTS transients. If the thermal emission rates would follow an exponential path, in the Arrhenius plot a line with a negative slope would appear. The value of this slope can directly be linked to the activation energy of the process and compared to the DLTS activation energies. However, as we have seen in Section 4.2, the thermal emission rates follow an unphysical path and this would make it difficult to incorporate the results in an Arrhenius plot. However, the lowest and highest three temperatures do show a trend, which can be made visible in the Arrhenius plots shown in Figure 34.

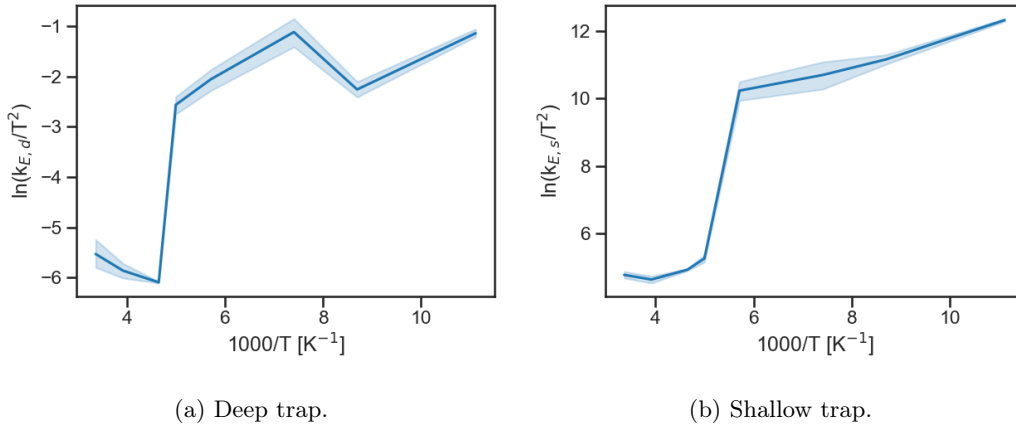


Figure 34: Arrhenius plots of the thermal emission rates for the deep and shallow trap states.

Take for example the trend shown in the bottom-left corner of Figure 34a, the slope can be estimated to have a value of about -2. If we take an activation energy of around 150 meV, which we observed for the DLTS results, in a semilog plot with  $1000/T$  as the x-axis, the slope can be calculated using the Boltzmann constant to have a value of about -18.4. The slope is directly proportional to the value of the activation energy, so even for the lowest calculated activation energy value from the long filling pulse DLTS measurements of around 30 meV, the slope would still be at least twice as high as the observed trend. Considering this particular trend is the highest visible slope observed in Figure 34, besides the abrupt decrease in the emission rate, which has been assigned to limitations in the parameter boundaries and not to actual physical processes in the measured material. Furthermore, the temperature dependency of the electron capture cross-section, which was shown to be exponential in Equation (4), was not taken into account in Figure 34. Since this T-dependency would include a prefactor 2 with the activation energy, the slope of the DLTS would have to be doubled to match the activation energy slopes of the TRMC, which would only increase the difference between the two activation energies even more.

Another point that must be considered is that the transients for the DLTS measurements only become visible at temperatures exceeding 255 K. In the case that these transients are caused by the emission of electronic traps, that should mean that in the TRMC analysis only for temperatures starting from this value the emission rate should start to increase heavily. What is seen, however, is that the emission rates for both traps are present even at the lowest temperatures and they do not show the heavy increase at the last two temperature steps, 255 K and 297 K respectively. The first attempt at increasing the parameter boundaries did not result in the expected exponential increase of the emission rates, especially visible at the high temperatures, thus more efforts must be made. This inconsistency can be due

to either measurement method and the used analysis and thus further research is needed to investigate this.

A definite answer to the research question can thus not be given, due to the complications of the analysis of the results from both measurement methods. The extracted activation energies clearly do not match, and for the DLTS measurements, there are strong indications that the origin of at least one of the exponential contributions to the transient is ion drift instead of electronic emission from trap states. However, in the next section, there are several methods proposed that could lead to a better comparison between the two measurement setups.

## 6 Outlook

The outlook of this thesis covers the proposed solutions for the bottlenecks in the analysis of both methods that were applied. First, the TRMC method will be discussed, based on the results discussed in Section 4.2.

### TRMC

#### Measurement methodology

Before focusing on the results from the individual parameters that were extracted from the fit and the suitability of the kinetic model, there are a couple of global actions that can be made to improve the fitting of this data set. For the current fits, only the traces measured using the cavity cell were used, so for a start, the open cell data should be included as well. In this way, the illumination intensity range will be extended by almost two orders of magnitude and this allows for better distinction between the intensity ranges where trap-assisted recombination dominates or the direct recombination. The illumination intensity where the dynamics transition from the first to the latter, can be linked to the concentration of electronic defects present in the material. This would allow for improved extraction of the electron mobility value since for trap-assisted recombination dominated regimes, these trapped charge carriers do not contribute significantly to the TRMC signal.

The quality of the fitting can also be improved by including the short timescale measurements, where the first microsecond of the decay is measured with a higher temporal resolution since for these fits only the longer measurement of the first 10 microseconds was used. However, even at this longer timescale, information about the decay of the conductance is lost, since the measurement cuts off when the decay dynamics are still in full effect. This is especially visible for the cavity measurement at lower temperatures and for these cases, it is recommended to measure at even longer timescales. The repetitions rate of the measurements is 10 Hz, so in theory, a measurement of 100 milliseconds would be the longest possible measurement. A suitable set of timescales should be chosen such that the initial photogeneration of free charge-carrier is captured as well as the full decay of these charge-carriers towards the equilibrium situation in dark. From these full sets of traces, the lifetime of the charge carriers can be calculated and by using the mobility values the diffusion length can be calculated using Equation (1). By plotting the concentrations of free holes and electrons over time respectively, the lifetime of each charge-carrier species can be distinguished. As mentioned before, for this a broader range of illumination intensities is needed to distinguish between the hole and electron mobility values.

Another manner to get a better insight into how the system changes over temperature is by reducing the temperature step size. Especially for the comparison with the DLTS measurements, this may be effective, since in that method a step size of 8 K is used, while for the current set of TRMC traces this step size is in the order of 40 K. This has to do with the increased temperature range, but this can also be adjusted to match the range used for the DLTS measurements.

To obtain better statistics on the measurement results, multiple samples that were made during the same preparation should be measured using the TRMC setup. In this way, one can make a stronger case about the material properties of samples from the same batch showing similar behaviour during the conductance measurements.

#### Fitting parameter boundaries

The results of the extracted parameter values from the TRMC measurements also point to particular directions to improve the fitting of the data. A straightforward improvement would be to increase the parameter value boundaries since for several of the parameters it is clear that the value is clipping to either of the parameter value boundaries. This is for example clear in the values for the defect concentrations and the concentration of excess holes. For the latter, the current boundaries are more restrictive than the physical possibility of the concentration, which can span from  $10^{13}$  to  $10^{17} \text{ cm}^{-3}$ , while it is currently restricted to only one order of magnitude. These strict parameter boundaries were implied when a different fitting method was applied, but this fitting algorithm allows for wider

parameter domains. First attempts were made at this, but ideally, for each process, it must be investigated what range of values would be physically possible and the parameter boundaries should be set accordingly. This would lead the fitting algorithm to look in directions that make physical sense, but in any case, with increasing parameter boundaries the chances increase that fits with a low residual value will be found for multiple different combinations of parameter values. These so-called 'local minima' will have to be traced and taken into account when discussing the resulting parameter values, since the values that yield a good solution may deviate significantly from one another. This was attempted for a single temperature step by taking four different sets of runs and the resulting parameter values deviated mutually significantly.

The way the fitting algorithm is currently set up is that it varies each of the twelve parameters values for each iteration over the parameter space that is defined by the set boundaries. After the given number of iterations has been completed, the resulting parameter values are obtained by averaging over the values in the 50 iterations that have the lowest residual value. With the current set of parameter boundaries, the error margin is low within the average. This can mean a couple of things, namely that there exists only one combination of parameters that fits the data well, or there might exist multiple local minima, but the best fits of these respective minima have a larger residual value than the 50 best fits from the best-fitting local minimum. In this manner, the other local minima might exist, but they don't become visible. However, for an increasing parameter space, there might co-exist multiple local minima with same-valued residuals, which would increase the standard deviation in the average over the 50 best fits. Performing data analysis to find these local minima is difficult to visualise since there are 12 parameters that are allowed to change. A possible method to localise the minima is to calculate the change in the residual value when moving from one iteration to another since around a certain minimum the derivative with respect to the 12 changing parameters should become close to zero when the minimum is reached. Some additional mathematics would be required to distinguish two minima from one another, using the ability of the fitting algorithm to distinguish between reaching a low point in the residual value compared to reaching some sort of residual 'plateau', where the derivative might be close to zero as well, but the residual is neither low nor reaching a minimum. To implement this a mathematical approach is necessarily combined with careful data analysis.

## Mobility

Parameter values extracted from the TRMC fits that might be limited by the parameter boundaries are among others the mobility values and in particular, the hole mobility. However, using qualitative observations of the TRMC traces, there is a strong indication that this value is actually physically limited at lower temperatures. The data shows that the mobility values are thermally reduced since the mobility is limited by acoustic phonon scattering, but this relation does not hold below 175 K, since there the mobility remains more or less stable. We have discussed what might cause this, but to distinguish between the different explanations, additional measurements can be performed on the material. In the case of the mobility being limited by a phase transition inside the material, one can do measurements to confirm whether this phase transition is actually taking place. The first measurement that could reveal the transition of the material from the perovskite cubic phase to the perovskite tetragonal phase is measuring the XRD patterns at low temperatures. When the material indeed transitions to the tetragonal phase, this would show in the peak splitting of the (100) and (200) peaks, making this a suitable method to detect an occurring phase transition. Another possible measurement method is by applying Differential Scanning Calorimetry (DSC), where the amount of energy to heat a sample is measured as a function of temperature. When a phase transition occurs with varying temperatures, the amount of energy needed to heat the system will be increased or lowered, depending on if the phase transition is endothermic or exothermic respectively. This method however only tracks if a phase transition occurs, but leaves no information on what the actual structure of the material is, so low-temperature XRD measurements would be the preferred option.

Another explanation was given for the mobility values at lower temperatures involving the wrongly assigned unity value to the free charge-carrier yield. A possible way to investigate this is to perform conductance measurements on the same sample using Pulse-

Radiolysis TRMC (PR-TRMC), where the charge-carriers are generated upon interaction with high energy electrons instead of being photogenerated. Due to the high energy of the electrons, each interaction will have enough energy to break the bonds that prevent charge-carriers from moving around free independent of each other and for these measurements the yield will be constant across the whole temperature range. Another option to detect the increased presence of excitons at lower temperatures is to measure the absorption spectrum at low temperatures. If the thermal energy of the material is insufficient to break up all exciton bonds, the increased concentration of excitons will cause a higher absorption at the absorption onset of the material, creating the distinctive excitonic feature in the absorption onset [78]. In this case adding a thermally activated exciton to the kinetic model would be suitable.

### Kinetic model

Before moving on to the outlook for the DLTS method, a general remark for the used TRMC kinetic model must be made. All possible improvements mentioned above are built upon the assumption that the current kinetic model is valid for the material of choice, however, if one takes a look at the fitted traces of for example Figures 18 and 19 a reoccurring fitting issue stands out. For the initial decay, the slope is too steep, then it bends towards the second slope less smoothly than the measurement and the second slope is again too steep. The improvement of following the smooth bending of the measured curves was improved by moving from a single trap model as used in previous TRMC studies, towards the proposed kinetic model involving two trap states. However, it seems like there is still a process not taken into account which affects the decay of the conductance inside the material. If this is caused by yet another electronic defect, can be investigated for further research, but up until then it must be kept in mind that the current kinetic model has a certain limitation in describing the decay of the photo-generated charge carriers. Finally, it must be noted that 12 parameters that are allowed to change freely inside the set boundaries is a high number for a fitting algorithm and this can lead easily to multiple local minima. For some of the parameter values, such as the emission rates, the physical temperature dependence is known, so implementing this in the kinetic model does both provide more reliable physical results and reduces the amount of freedom the fitting algorithm has in finding a fit.

## DLTS

### Parameter correlation

From the DLTS measurements and the fitting of this data, the possible correlation between the assigned  $c_i$  and  $E_{A,i}$  values was one thing that stood out. The reason for this could have been that during the fitting process the fitting algorithm was only looking for certain combinations between the two that followed the curves that were visible in Figure 31. By looking at the full range of repetitions in Figure 32, it was shown that this was not the case, but it confirmed that around a certain local minimum, this correlation does exist. A proposed adaption to the fitting algorithm would be to allow the fitting process to deviate from these curves, even when a certain local minimum is reached. This could be done by momentarily increasing the mutation value of the fitting algorithm, such that the system moves out of the minimum and looks for a suitable fit in a different region. Another possibility is to save the values of the fit for each iteration, such that one can make a scatter plot over the entire parameter space that the fitting algorithm looks for. If the fitting algorithm actually only looks for certain combinations of  $c$ -values and activation energies, this will show in the absence of scatter points at a certain domain the fitting algorithm misses. If the fitting covers the whole domain, one can investigate where the fits are located with the lowest residual using the colour map, where a darker colour indicates a better fit. In this way, it could be confirmed that the fitting algorithm only finds its best fits along a certain curve in the parameter domain. If one could visualise the fitting process by allowing the scatter points to appear in order of the iteration steps, then it would become clearer how the system works towards a certain fitting minimum.

Another explanation for the apparent correlation between the  $c$ -values and the activation energies could be that the temperature range over which the transients are analysed is too

small to properly extract the activation energy. By having a too large temperature step, the precise temperature from which the capacitance transient becomes visible might be missed, thus leading to an inaccurate determination of the activation energy. This could also be understood using an Arrhenius plot. If we were to plot the emission rates in an Arrhenius plot, for a small temperature range the points would be clustered together and determining the linear slope of the temperature dependency of the measured rates would be prone to high uncertainties. In the case of such noisy results, a small slope would yield a low activation energy and the line drawn through the points would cross the y-axis at a relatively low value. The value of the y-axis at this crossing point is determined by the  $c$ -value, thus also this value would become small. In the case of a steeper slope, the activation energy would be higher and due to the increased height of the crossing point of the line with the y-axis, the assigned  $c$ -value would increase as well. By measuring for a broader temperature range, the uncertainty in determining the slope could be reduced drastically and the assigned activation energies and  $c$ -values could be better defined. However, the difficulty here lies in the fact that below 255 K the current devices do not show a capacitance transient, thus only at the higher temperatures the temperature range could be increased. At temperatures exceeding 330 K, the thermal stability of the material should theoretically still hold, but this must be considered when increasing the temperature range.

## 7 Conclusion

The goal of this thesis was to investigate the temperature-dependency of the charge-carrier dynamics in all-inorganic mixed-halide perovskite thin films. In particular, the influence of electronic intermediate band trap states was of interest and how the trapping, emission and trap-assisted non-radiative recombination rates behaved under varying temperatures. To achieve this the perovskite thin film was measured using the TRMC method and DLTS measurements were performed on a PSC device with this type of perovskite material as the photoactive layer. The main idea was to compare the extracted thermal emission rates and the corresponding activation energies from both methods, if these would match then this would make a strong case that the same electronic processes are probed using either method. However, using the end results of both measurement methods we were unable to match the extracted activation energies from the DLTS fits to either of the proposed trap states in the kinetic model from the TRMC. This mismatch can have multiple causes, such as that the results of the TRMC showed many inconsistencies, with nonphysically large changes in the extracted parameters over varying temperatures. One cause for this is believed to be the too restrictive parameter boundary values, but the first attempts at increasing the parameter boundaries show that this approach is not straightforward and a physical approach should be taken to determine how the parameter values should change over temperature. For the extracted emission rates from both the trap states in the kinetic model that is applied, a thermally activated trend is visible for certain temperature intervals, but due to the sudden drops in this value at increasing temperatures in the mid-range of the measured temperatures, the Arrhenius plot made from these emission rates does not show a linear trend across the entire temperature range. The slopes of the emission rates plotted of a subrange of the measured temperatures did also not match the slope corresponding to the extracted activation energies from the DLTS method. This could be due to the large uncertainty due to the sparse temperature points, but it could also be that the DLTS measurements actually captures the capacitance transients caused by non-electronic processes, like ion drift. A strong indication for this is that for both the short and long filling pulse, two exponentials can be used to successfully fit the data, indicating that in both measurements two processes are present. Since for a longer filling pulse, the ion drift is expected to influence the capacitance of the device, this process could in a lesser amount already be present at the short filling pulse. It is thus difficult to draw conclusions on the comparison between the two methods since the difference between the outcomes can have many different causes. However, in the Outlook, multiple ways were proposed to improve either technique and how to obtain more trustworthy results by fitting the measured traces, such as increasing the parameter boundaries of the TRMC fitting or decreasing the temperature steps taken in both TRMC and DLTS to enhance the extraction of the activation energies. This could lead to better insights on how to match the results of both measurement setups and this could reveal significant information on the charge-carrier dynamics of this type of material. One of these improvements might be to increase the temperature range to higher temperatures, additional to using the smaller temperature steps, which will reduce the uncertainty in the extraction of physical parameters from the measurements, but it will simultaneously test the thermal stability of the material, which is one of the main merits compared to the organic-inorganic perovskite materials. Hopefully, in follow-up studies these proposed improvements will be taken into account and lead to better insights into the behaviour of charge-carriers in the all-inorganic mixed-halide perovskite thin films, paving the way for a broad range of applications, resisting thermally challenging conditions.

## 8 Acknowledgements

For the acknowledgements, I would like to start thanking the two supervisors that guided me through this master thesis. First I would like to thank **Tom Savenije** from the TU Delft for making it possible for me to start on this collaborative effort with AMOLF and for the engaging and enjoyable discussions we had on the nature of this interesting perovskite material. My thanks go to **Bruno Ehrler** as well, who allowed me to become a part of his group at AMOLF and who challenged me during the numerous work discussions by sharing his scientific insights about my project. I want to express my gratitude towards my daily supervisors, **Jiashang Zhao** at the TU Delft and **Moritz Schmidt** at AMOLF, for the persistent guidance they provided during this master thesis. **Jiashang** introduced me to the world of perovskites and, using her expertise, we ploughed through the production a good number of sample batches in order to make the desired TRMC measurements possible. **Moritz** has provided me with theoretical insights about the complex capacitance-based DLTS measurement method during our interesting conversations and his programming skills were indispensable for the development of the fitting algorithm for the TRMC measurements. I want to thank **Lucie** for the enjoyable conversations that shone a light on the interpretation of my results at AMOLF. Without the incredible fitting algorithm of **Gianluca**, the analysis of the results would not have been possible, so I want to thank him for that and for his insightful knowledge about charge-carrier dynamics. Furthermore, I want to thank **María** for the new point of view for the interpretation of the TRMC results. Without the help of the technicians I wouldn't have been able to do anything, so I want to thank **Nick**, **Jos** and **Wiel** for taking great care of the setups in Delft, while **Marc** did an amazing job by solving the issues in the lab at AMOLF that allowed the whole group to continue doing science. My project would not have been as interesting and fun if it wasn't for my fellow Master students, so I want to thank **Jasmeen**, **Oscar**, **Toon**, **Rens**, **Daan** and **David** for the conversations and laughs we had along the way. At last, I want to thank the whole **Hybrid Solar Cells** group for welcoming me and for providing such an open and pleasant working environment. I am really grateful that I could join the group rail trip during the final weeks of my project as the cherry on the cake, the memories of which I will cherish for a long time to come.



## References

- [1] Rebecca Lindsey and LuAnn Dahlman. *Climate change: Global temperature*. Mar. 2021. URL: <https://www.climate.gov/news-features/understanding-climate/climate-change-global-temperature>.
- [2] Veronika Eyring et al. “Human Influence on the Climate System: Contribution of Working Group I to the Sixth Assessment Report of the Intergovernmental Panel on Climate Change”. In: *IPCC Sixth Assessment Report* (2021).
- [3] Paris Agreement. “Paris agreement”. In: *Report of the Conference of the Parties to the United Nations Framework Convention on Climate Change (21st Session, 2015: Paris)*. Retrived December. Vol. 4. HeinOnline. 2015, p. 2017.
- [4] IEA. *Global Energy Review 2021 – analysis*. 2021. URL: <https://www.iea.org/reports/global-energy-review-2021>.
- [5] Dennis L Hartmann. *Global physical climatology*. Vol. 103. Newnes, 2015.
- [6] Alessandro Clerici and G Alimonti. “World energy resources”. In: *EPJ WEB of conferences*. Vol. 98. EDP Sciences. 2015, p. 01001.
- [7] Simon Phillips and Werner Warmuth. *Photovoltaics report - Fraunhofer ISE Simon*. July 2021. URL: <https://www.ise.fraunhofer.de/en/publications/studies/photovoltaics-report.html>.
- [8] Ewan D Dunlop. “Lifetime performance of crystalline silicon PV modules”. In: *3rd World Conference on Photovoltaic Energy Conversion, 2003. Proceedings of*. Vol. 3. IEEE. 2003, pp. 2927–2930.
- [9] Lucio Claudio Andreani et al. “Silicon solar cells: toward the efficiency limits”. In: *Advances in Physics: X* 4.1 (2019), p. 1548305.
- [10] Klaus-Dieter Jäger et al. *Solar energy: fundamentals, technology and systems*. UIT Cambridge, 2016.
- [11] Albert Polman et al. “Photovoltaic materials: Present efficiencies and future challenges”. In: *Science* 352.6283 (2016).
- [12] Akihiro Kojima et al. “Organometal halide perovskites as visible-light sensitizers for photovoltaic cells”. In: *Journal of the American Chemical Society* 131.17 (2009), pp. 6050–6051.
- [13] Hanul Min et al. “Perovskite solar cells with atomically coherent interlayers on SnO<sub>2</sub> electrodes”. In: *Nature* 598.7881 (2021), pp. 444–450.
- [14] NREL gov. *Best research-cell efficiency chart*. 2021. URL: <https://www.nrel.gov/pv/cell-efficiency.html>.
- [15] Youwei Wang et al. “High intrinsic carrier mobility and photon absorption in the perovskite CH<sub>3</sub>NH<sub>3</sub>PbI<sub>3</sub>”. In: *Physical Chemistry Chemical Physics* 17.17 (2015), pp. 11516–11520.
- [16] Sneha A Kulkarni et al. “Band-gap tuning of lead halide perovskites using a sequential deposition process”. In: *Journal of Materials Chemistry A* 2.24 (2014), pp. 9221–9225.
- [17] *Oxford PV hits New World Record for Solar Cell*. URL: <https://www.oxfordpv.com/news/oxford-pv-hits-new-world-record-solar-cell>.
- [18] Qi Chen et al. “Planar heterojunction perovskite solar cells via vapor-assisted solution process”. In: *Journal of the American Chemical Society* 136.2 (2014), pp. 622–625.
- [19] Kang Wang et al. “All-inorganic cesium lead iodide perovskite solar cells with stabilized efficiency beyond 15%”. In: *Nature communications* 9.1 (2018), pp. 1–8.
- [20] Jing Wang et al. “Highly efficient all-inorganic perovskite solar cells with suppressed non-radiative recombination by a Lewis base”. In: *Nature communications* 11.1 (2020), pp. 1–9.
- [21] Zijun Yi et al. “Will organic–inorganic hybrid halide lead perovskites be eliminated from optoelectronic applications?” In: *Nanoscale Advances* 1.4 (2019), pp. 1276–1289.

- [22] Federico Bella et al. “Caesium for perovskite solar cells: an overview”. In: *Chemistry–A European Journal* 24.47 (2018), pp. 12183–12205.
- [23] AB Djurišić et al. “Perovskite solar cells-An overview of critical issues”. In: *Progress in Quantum Electronics* 53 (2017), pp. 1–37.
- [24] T. Jesper Jacobsson et al. “Exploration of the compositional space for mixed lead halogen perovskites for high efficiency solar cells”. In: *Energy & Environmental Science* 9.5 (2016), pp. 1706–1724. DOI: [10.1039/c6ee00030d](https://doi.org/10.1039/c6ee00030d).
- [25] Eline M Hutter et al. “Vapour-deposited cesium lead iodide perovskites: microsecond charge carrier lifetimes and enhanced photovoltaic performance”. In: *ACS energy letters* 2.8 (2017), pp. 1901–1908.
- [26] Laura M Herz. “Charge-carrier mobilities in metal halide perovskites: fundamental mechanisms and limits”. In: *ACS Energy Letters* 2.7 (2017), pp. 1539–1548.
- [27] Qingsen Zeng et al. “Inorganic cspbi2BR perovskite solar cells: The progress and perspective”. In: *Solar RRL* 3.1 (2018), p. 1800239. DOI: [10.1002/solr.201800239](https://doi.org/10.1002/solr.201800239).
- [28] Chang Yi et al. “Intermediate-phase-assisted low-temperature formation of  $\gamma$ -CsPbI<sub>3</sub> films for high-efficiency deep-red light-emitting devices”. In: *Nature communications* 11.1 (2020), pp. 1–8.
- [29] Weijie Chen et al. “Precise control of crystal growth for highly efficient CsPbI<sub>2</sub>Br perovskite solar cells”. In: *Joule* 3.1 (2019), pp. 191–204. DOI: [10.1016/j.joule.2018.10.011](https://doi.org/10.1016/j.joule.2018.10.011).
- [30] Chuan-Liang Chen et al. “Improved open-circuit voltage and ambient stability of cspbi2br perovskite solar cells by incorporating ch<sub>3</sub>nh<sub>3</sub>cl”. In: *Rare Metals* 39.2 (2019), pp. 131–138. DOI: [10.1007/s12598-019-01341-z](https://doi.org/10.1007/s12598-019-01341-z).
- [31] Bart Roose et al. “Critical assessment of the use of excess lead iodide in lead halide perovskite solar cells”. In: *The Journal of Physical Chemistry Letters* 11.16 (2020), pp. 6505–6512.
- [32] Jia Li et al. “Potassium Acetate-Based Treatment for Thermally Co-Evaporated Perovskite Solar Cells”. In: *Coatings* 10.12 (2020), p. 1163.
- [33] Eline M. Hutter et al. “Thermodynamic stabilization of mixed-halide perovskites against phase segregation”. In: *Cell Reports Physical Science* 1.8 (2020), p. 100120. DOI: [10.1016/j.xcrp.2020.100120](https://doi.org/10.1016/j.xcrp.2020.100120).
- [34] Huichao Zhang et al. “Phase segregation due to ion migration in all-inorganic mixed-halide perovskite nanocrystals”. In: *Nature communications* 10.1 (2019), pp. 1–8.
- [35] Yanbo Shang et al. “Efficient and photostable CsPbI<sub>2</sub>Br solar cells realized by adding PMMA”. In: *Journal of Semiconductors* 42.5 (2021), pp. 050501–050501.
- [36] Fang He et al. “Highly crystalline cspbi2br films for efficient perovskite solar cells via compositional engineering”. In: *RSC Advances* 9.52 (2019), pp. 30534–30540. DOI: [10.1039/c9ra06363c](https://doi.org/10.1039/c9ra06363c).
- [37] Sebastian Engmann et al. “Higher order effects in organic leds with sub-bandgap turn-on”. In: *Nature Communications* 10.1 (2019). DOI: [10.1038/s41467-018-08075-z](https://doi.org/10.1038/s41467-018-08075-z).
- [38] Michael D Irwin et al. “p-Type semiconducting nickel oxide as an efficiency-enhancing anode interfacial layer in polymer bulk-heterojunction solar cells”. In: *Proceedings of the National Academy of Sciences* 105.8 (2008), pp. 2783–2787.
- [39] Wei Ping Chu et al. “Using intrinsic layer to improve the efficiency of organic solar cells”. In: *PIERS Online* 3.6 (2007), pp. 825–828.
- [40] Yuya Yokokura et al. “Control of indium tin oxide anode work function modified using Langmuir-Blodgett monolayer for high-efficiency organic photovoltaics”. In: *AIP Advances* 7.8 (2017), p. 085321.
- [41] Zafar Abas et al. “Electrode effects of a cellulose-based electro-active paper energy harvester”. In: *Smart materials and structures* 23.7 (2014), p. 074003.
- [42] Jeihyun Lee et al. “Electron transport mechanism of bathocuproine exciton blocking layer in organic photovoltaics”. In: *Physical Chemistry Chemical Physics* 18.7 (2016), pp. 5444–5452.

- [43] Yuxuan Chen et al. “The distinctive phase stability and defect physics in CsPbI<sub>2</sub>Br perovskite”. In: *Journal of Materials Chemistry A* 7.35 (2019), pp. 20201–20207.
- [44] Jarvist M Frost and Aron Walsh. “What is moving in hybrid halide perovskite solar cells?”. In: *Accounts of chemical research* 49.3 (2016), pp. 528–535.
- [45] Zhuo Yang et al. “Impact of the Halide Cage on the Electronic Properties of Fully Inorganic Cesium Lead Halide Perovskites”. In: *ACS Energy Letters* 2 (July 2017), p. 1621. DOI: [10.1021/acsenergylett.7b00416](https://doi.org/10.1021/acsenergylett.7b00416).
- [46] Donald A. Neamen. *Semiconductor physics and devices: Basic principles*. McGraw-Hill, 2012.
- [47] Samiya Mahjabin et al. “Perceiving of defect tolerance in perovskite absorber layer for efficient perovskite solar cell”. In: *IEEE Access* 8 (2020), pp. 106346–106353.
- [48] Xie Zhang, Mark E. Turiansky, and Chris G. Van de Walle. “Correctly assessing defect tolerance in halide perovskites”. In: *The Journal of Physical Chemistry C* 124.11 (2020), pp. 6022–6027. DOI: [10.1021/acs.jpcc.0c01324](https://doi.org/10.1021/acs.jpcc.0c01324).
- [49] WTRW Shockley and WT Read Jr. “Statistics of the recombinations of holes and electrons”. In: *Physical review* 87.5 (1952), p. 835.
- [50] Jiashang Zhao et al. “How Deep Hole Traps Affect the Charge Dynamics and Collection in Bare and Bilayers of Methylammonium Lead Bromide”. In: *ACS applied materials & interfaces* 13.14 (2021), pp. 16309–16316.
- [51] Xiaopeng Zheng et al. “Defect passivation in hybrid perovskite solar cells using quaternary ammonium halide anions and cations”. In: *Nature Energy* 2.7 (2017), pp. 1–9.
- [52] Qi Jiang et al. “Surface passivation of perovskite film for efficient solar cells”. In: *Nature Photonics* 13.7 (2019), pp. 460–466.
- [53] Qian Zhou et al. “Understanding Temperature-Dependent Charge Extraction and Trapping in Perovskite Solar Cells”. In: *Advanced Functional Materials* 30.22 (2020), p. 2000550.
- [54] Ke Wei et al. “Temperature-dependent excitonic photoluminescence excited by two-photon absorption in perovskite CsPbBr<sub>3</sub> quantum dots”. In: *Optics letters* 41.16 (2016), pp. 3821–3824.
- [55] Eline M Hutter et al. “Direct–indirect character of the bandgap in methylammonium lead iodide perovskite”. In: *Nature materials* 16.1 (2017), pp. 115–120.
- [56] Ivan Pelant and Jan Valenta. *Luminescence spectroscopy of semiconductors*. Oxford University Press, 2012.
- [57] Hee Chul Woo et al. “Temperature-dependent photoluminescence of CH<sub>3</sub>NH<sub>3</sub>PbBr<sub>3</sub> perovskite quantum dots and bulk counterparts”. In: *The journal of physical chemistry letters* 9.14 (2018), pp. 4066–4074.
- [58] Jiaming Li et al. “Temperature-dependent photoluminescence of inorganic perovskite nanocrystal films”. In: *RSC advances* 6.82 (2016), pp. 78311–78316.
- [59] Michael J Trimpl et al. “Charge-carrier trapping and radiative recombination in metal halide perovskite semiconductors”. In: *Advanced Functional Materials* 30.42 (2020), p. 2004312.
- [60] Shreetu Shrestha et al. “Assessing temperature dependence of drift mobility in methylammonium lead iodide perovskite single crystals”. In: *The Journal of Physical Chemistry C* 122.11 (2018), pp. 5935–5939.
- [61] Jie Ma and Lin-Wang Wang. “The nature of electron mobility in hybrid perovskite CH<sub>3</sub>NH<sub>3</sub>PbI<sub>3</sub>”. In: *Nano letters* 17.6 (2017), pp. 3646–3654.
- [62] Leqi Lin and NM Ravindra. “Temperature dependence of CIGS and perovskite solar cell performance: an overview”. In: *SN Applied Sciences* 2.8 (2020), pp. 1–12.
- [63] Rebecca L Milot et al. “Temperature-dependent charge-carrier dynamics in CH<sub>3</sub>NH<sub>3</sub>PbI<sub>3</sub> perovskite thin films”. In: *Advanced Functional Materials* 25.39 (2015), pp. 6218–6227.

- [64] Giovanni Landi et al. “Correlation between electronic defect states distribution and device performance of perovskite solar cells”. In: *Advanced Science* 4.10 (2017), p. 1700183.
- [65] Shuyan Shao et al. “Efficient perovskite solar cells over a broad temperature window: the role of the charge carrier extraction”. In: *Advanced Energy Materials* 7.22 (2017), p. 1701305.
- [66] Tom J Savenije et al. “Quantifying Charge-Carrier Mobilities and Recombination Rates in Metal Halide Perovskites from Time-Resolved Microwave Photoconductivity Measurements”. In: *Advanced Energy Materials* 10.26 (2020), p. 1903788.
- [67] DV Lang. “Deep-level transient spectroscopy: A new method to characterize traps in semiconductors”. In: *Journal of applied physics* 45.7 (1974), pp. 3023–3032.
- [68] Moritz H Futscher et al. “Quantifying mobile ions and electronic defects in perovskite-based devices with temperature-dependent capacitance measurements: Frequency vs time domain”. In: *The Journal of chemical physics* 152.4 (2020), p. 044202.
- [69] Johanna Siekmann, Sandheep Ravishankar, and Thomas Kirchartz. “Apparent Defect Densities in Halide Perovskite Thin Films and Single Crystals”. In: *ACS Energy Letters* 6.9 (2021), pp. 3244–3251.
- [70] Eric Jones, Travis Oliphant, Pearu Peterson, et al. *SciPy: Open source scientific tools for Python*. 2001–. URL: <http://www.scipy.org/>.
- [71] Guannan Yin et al. “Precursor Engineering for All-Inorganic CsPbI<sub>2</sub>Br Perovskite Solar Cells with 14.78% Efficiency”. In: *Advanced Functional Materials* 28.39 (2018), p. 1803269.
- [72] Yutao Wang et al. “Phase segregation in inorganic mixed-halide perovskites: from phenomena to mechanisms”. In: *Photon. Res.* 8.11 (Nov. 2020), A56–A71. DOI: [10.1364/PRJ.402411](https://doi.org/10.1364/PRJ.402411). URL: <http://www.osapublishing.org/prj/abstract.cfm?URI=prj-8-11-A56>.
- [73] Rebecca Saive. “S-Shaped current–voltage characteristics in solar cells: A review”. In: *IEEE journal of photovoltaics* 9.6 (2019), pp. 1477–1484.
- [74] Shou-En Chiang et al. “Origins of the s-shape characteristic in J–V curve of inverted-type perovskite solar cells”. In: *Nanotechnology* 31.11 (2019), p. 115403.
- [75] Anton Sundqvist et al. “Origin of the S-Shaped JV Curve and the Light-Soaking Issue in Inverted Organic Solar Cells”. In: *Advanced Energy Materials* 6.6 (2016), p. 1502265.
- [76] Rasha A Awni et al. “Influence of charge transport layers on capacitance measured in halide perovskite solar cells”. In: *Joule* 4.3 (2020), pp. 644–657.
- [77] Elizabeth Von Hauff. “Impedance spectroscopy for emerging photovoltaics”. In: *The Journal of Physical Chemistry C* 123.18 (2019), pp. 11329–11346.
- [78] Xihan Chen et al. “Excitonic effects in methylammonium lead halide perovskites”. In: *The journal of physical chemistry letters* 9.10 (2018), pp. 2595–2603.

## 9 Appendix

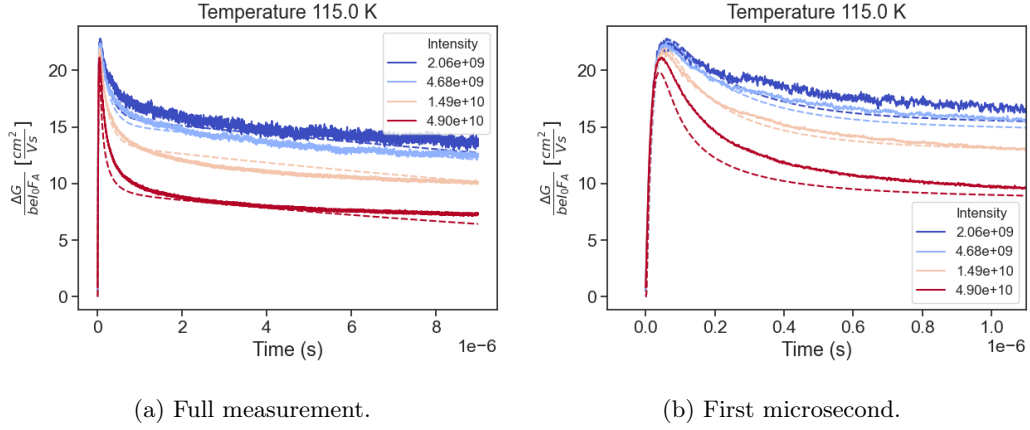


Figure 35: Measured and fitted TRMC traces at 115 K.

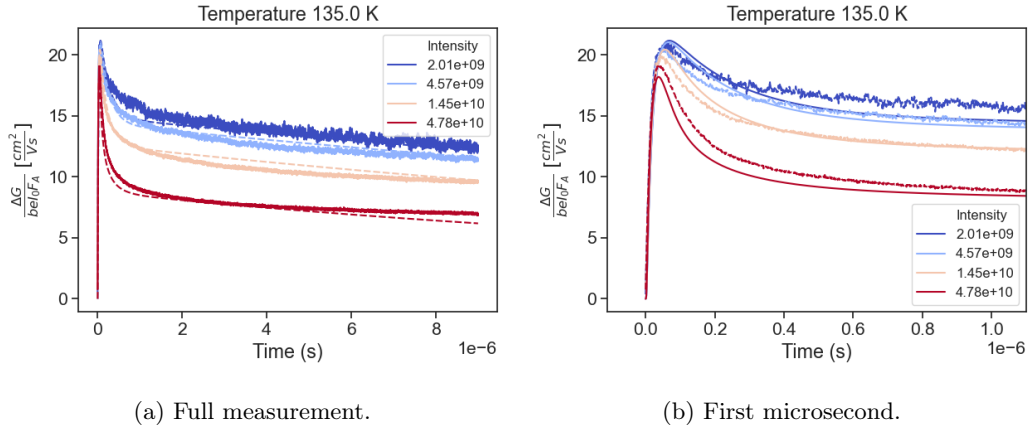


Figure 36: Measured and fitted TRMC traces at 135 K.

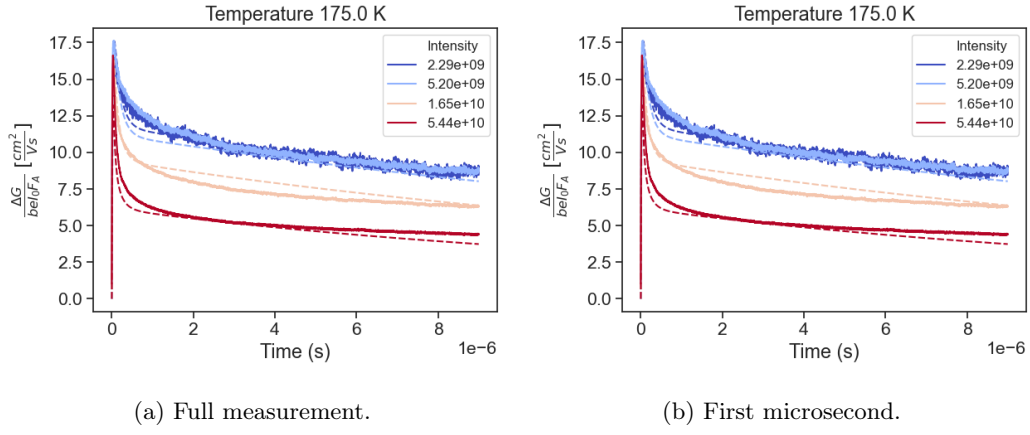


Figure 37: Measured and fitted TRMC traces at 175 K.

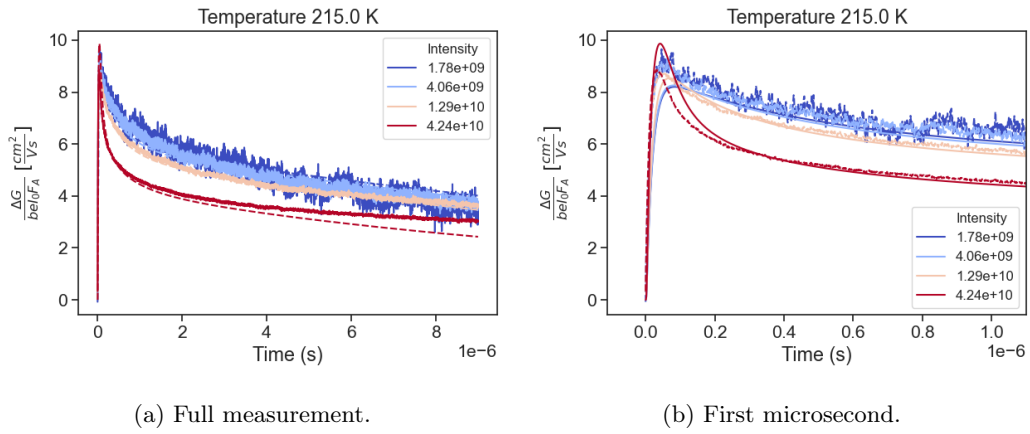


Figure 38: Measured and fitted TRMC traces at 215 K.

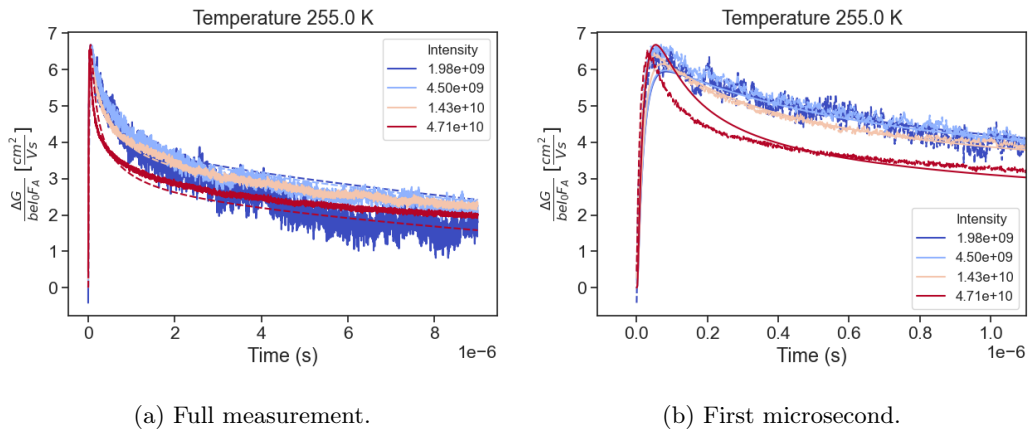
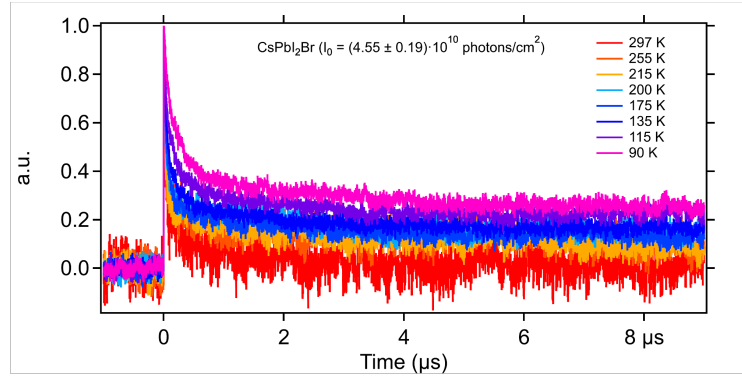
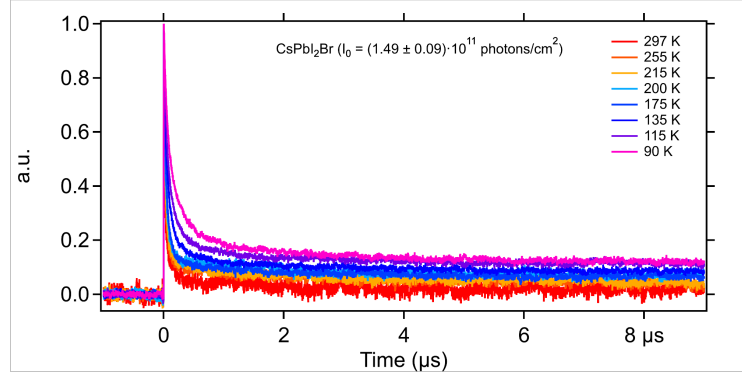


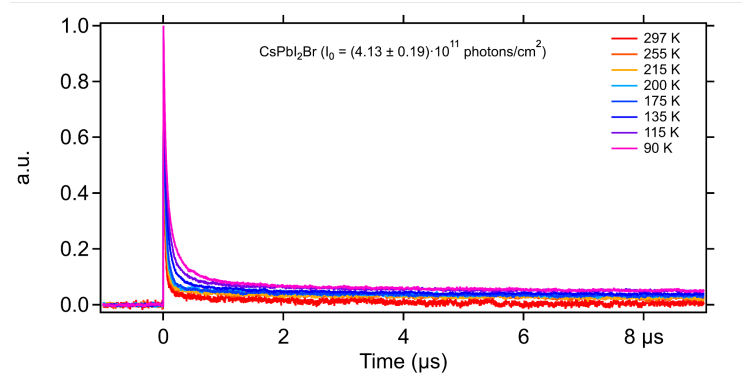
Figure 39: Measured and fitted TRMC traces at 255 K.



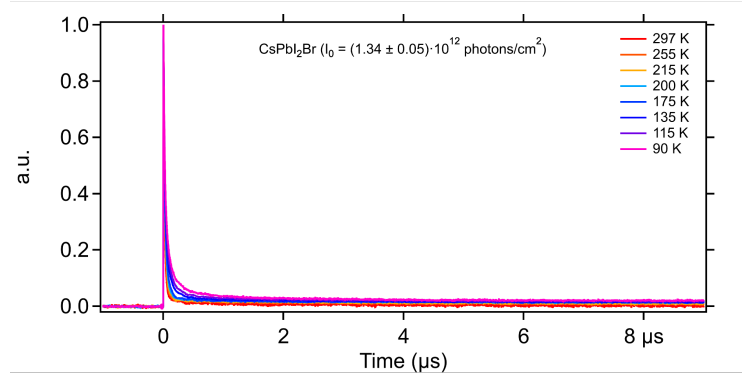
(a)  $I_0 \approx 4.6 \times 10^{10}$  photons/cm<sup>2</sup>



(b)  $I_0 \approx 1.5 \times 10^{11}$  photons/cm<sup>2</sup>



(c)  $I_0 \approx 4.1 \times 10^{11}$  photons/cm<sup>2</sup>



(d)  $I_0 \approx 1.3 \times 10^{12}$  photons/cm<sup>2</sup>

Figure 40: Temperature-dependent TRMC traces for fixed intensities, measured using an open cell.

<b>T</b>	<b>90</b>	<b>115</b>	<b>135</b>	<b>175</b>	<b>200</b>	<b>215</b>	<b>255</b>	<b>297</b>
$\mu_h$ ( $\text{cm}^2/(\text{V}\cdot\text{s})^{-1}$ )	27.32	28.07	26.32	22.59	14.36	9.41	6.84	6.42
$\mu_e$ ( $\text{cm}^2/(\text{V}\cdot\text{s})^{-1}$ )	15.80	15.64	20.05	23.07	18.80	18.06	7.55	8.39
$k_2$ ( $\times 10^{-8} \text{ cm}^3 \text{ s}^{-1}$ )	0.767	0.868	1.43	3.10	1.09	0.424	0.160	2.21
$p_0$ ( $\times 10^{14} \text{ cm}^{-3}$ )	5.03	5.80	5.62	5.52	9.75	9.99	20.0	5.37
$k_{T,d}$ ( $\times 10^{-8} \text{ cm}^3 \text{ s}^{-1}$ )	1.46	1.37	2.21	3.90	2.96	1.28	0.738	1.15
$k_{E,d}$ ( $\times 10^3 \text{ s}^{-1}$ )	2.70	1.57	6.56	4.86	3.56	0.104	0.227	0.629
$k_{R,d}$ ( $\times 10^{-11} \text{ cm}^3 \text{ s}^{-1}$ )	3.73	3.50	3.48	5.69	2.60	3.50	2.38	24.2
$N_{T,d}$ ( $\times 10^{14} \text{ cm}^{-3}$ )	9.68	9.45	9.58	8.87	9.95	9.98	9.87	9.16
$k_{T,s}$ ( $\times 10^{-7} \text{ cm}^3 \text{ s}^{-1}$ )	141	79.2	111	231	4.19	1.84	0.944	1.79
$k_{E,s}$ ( $\times 10^7 \text{ s}^{-1}$ )	185	105	95.4	121	0.819	0.635	0.717	1.10
$k_{R,s}$ ( $\times 10^{-11} \text{ cm}^3 \text{ s}^{-1}$ )	1.67	2.04	1.67	1.85	0.611	3.48	2.32	15.3
$N_{T,s}$ ( $\times 10^{14} \text{ cm}^{-3}$ )	9.65	6.15	5.53	5.76	4.04	6.74	6.66	6.37
$\chi^2$	90.07	24.05	47.18	43.31	11.08	37.53	30.82	51.57

Table 1: Parameter values from fitted TRMC traces.

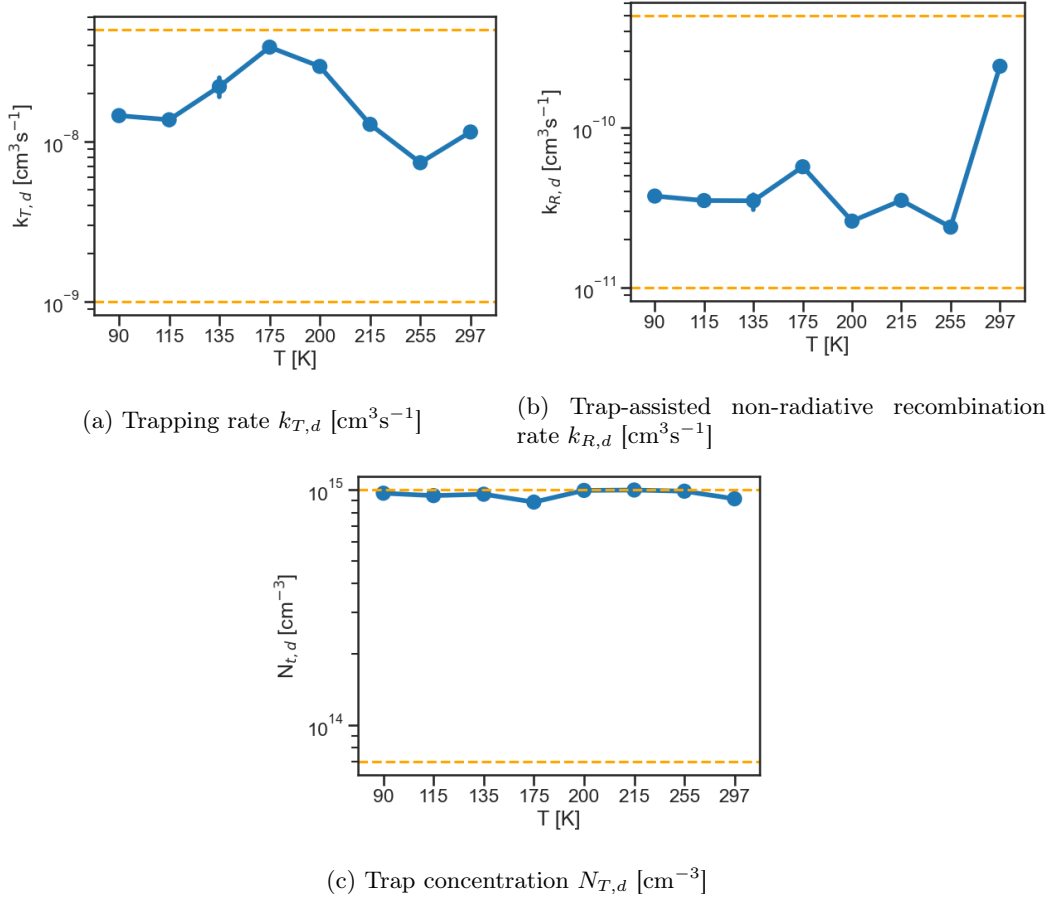


Figure 41: Deep trap fit parameter values plotted for varying temperatures.



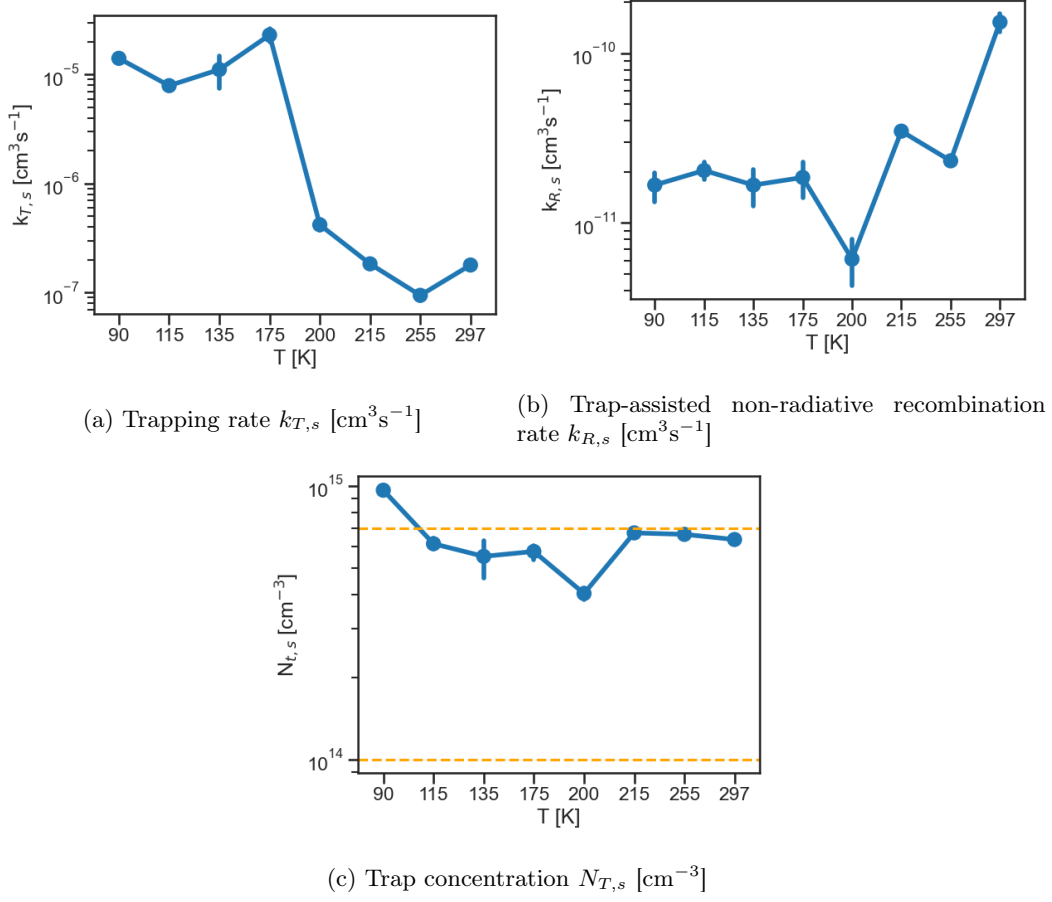


Figure 42: Shallow trap fit parameter values plotted for varying temperatures.

<b>T</b>	<b>90</b>	<b>115</b>	<b>135</b>	<b>175</b>	<b>200(1)</b>	<b>200(2)</b>	<b>200(3)</b>	<b>200(4)</b>	<b>215</b>	<b>255</b>	<b>297</b>
$\mu_h$ ( $\text{cm}^2/(\text{V}\cdot\text{s})^{-1}$ )	26.65	29.46	27.90	23.53	15.33	15.70	15.52	15.95	12.44	8.58	6.79
$\mu_e$ ( $\text{cm}^2/(\text{V}\cdot\text{s})^{-1}$ )	14.49	18.35	14.07	11.11	16.25	13.37	22.14	12.39	15.35	21.14	8.65
$k_2$ ( $\times 10^{-8} \text{cm}^3 \text{s}^{-1}$ )	3.04	47.51	37.36	46.46	48.80	42.90	48.01	47.12	37.62	48.20	26.81
$p_0$ ( $\times 10^{14} \text{cm}^{-3}$ )	2.63	3.61	3.54	3.20	6.76	5.48	7.91	5.52	14.12	48.11	3.98
$k_{T,d}$ ( $\times 10^{-8} \text{cm}^3 \text{s}^{-1}$ )	1.04	12.09	2.02	4.70	31.66	5.53	56.68	4.25	25.57	87.32	4.75
$k_{E,d}$ ( $\times 10^4 \text{s}^{-1}$ )	8.14	6.54	7.05	9.67	9.23	9.48	2.10	7.57	8.48	7.34	8.61
$k_{R,d}$ ( $\times 10^{-11} \text{cm}^3 \text{s}^{-1}$ )	0.312	0.526	0.206	0.294	0.240	0.714	2.93	1.59	1.80	0.548	23.57
$N_{T,d}$ ( $\times 10^{15} \text{cm}^{-3}$ )	3.25	3.33	14.62	6.16	2.45	11.67	1.61	14.29	3.71	2.91	2.11
$k_{T,s}$ ( $\times 10^{-4} \text{cm}^3 \text{s}^{-1}$ )	0.825	10.55	1.93	3.84	27.85	4.60	50.31	3.49	22.63	68.91	2.54
$k_{E,s}$ ( $\times 10^{10} \text{s}^{-1}$ )	6.48	6.15	3.09	3.78	0.989	3.62	1.68	3.03	6.52	0.270	1.80
$k_{R,s}$ ( $\times 10^{-12} \text{cm}^3 \text{s}^{-1}$ )	2.48	2.14	1.16	1.66	0.724	2.90	7.89	6.68	9.44	2.73	135
$N_{T,s}$ ( $\times 10^{15} \text{cm}^{-3}$ )	17.95	12.71	18.00	11.14	1.59	16.68	1.50	18.98	12.45	1.23	7.87
$\chi^2$	35.90	14.53	13.84	34.58	17.25	20.96	17.87	19.32	34.68	15.37	58.54

Table 2: Parameter values from fitted TRMC traces for wide parameter boundaries.

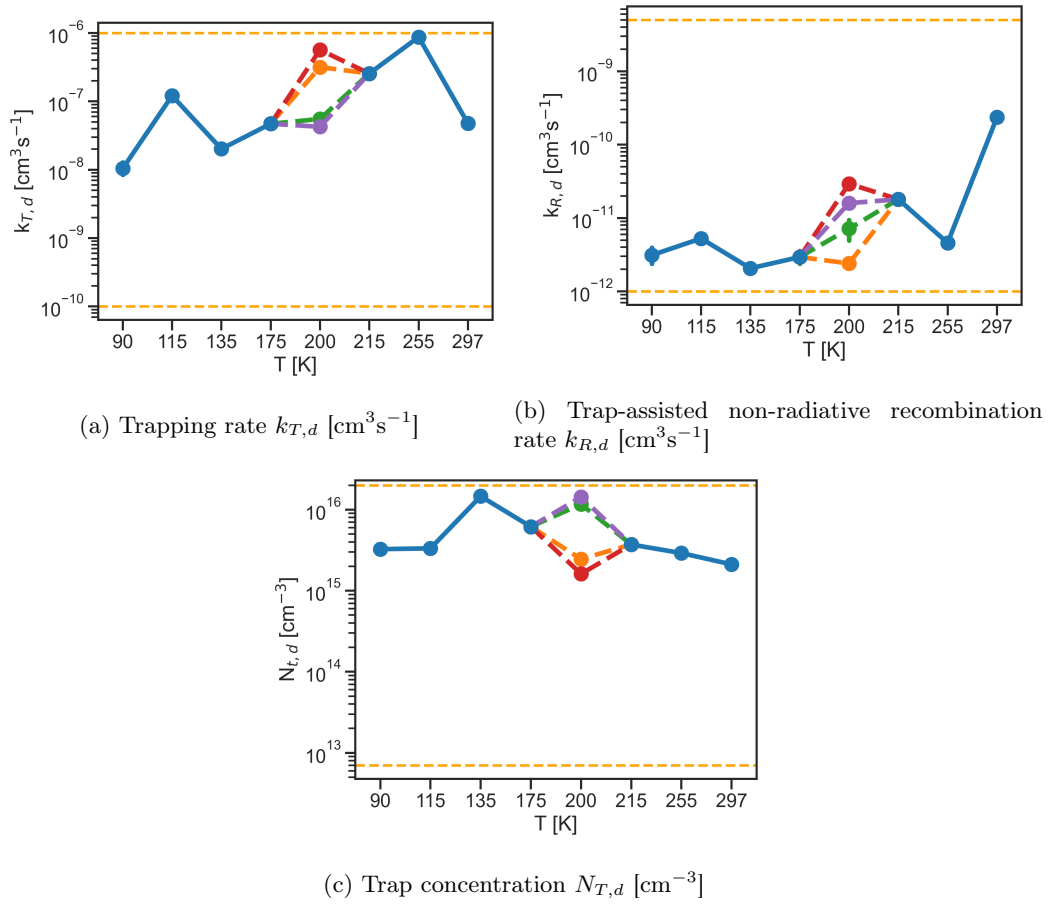


Figure 43: Deep trap fit parameter values plotted for varying temperatures using wide parameter boundaries.

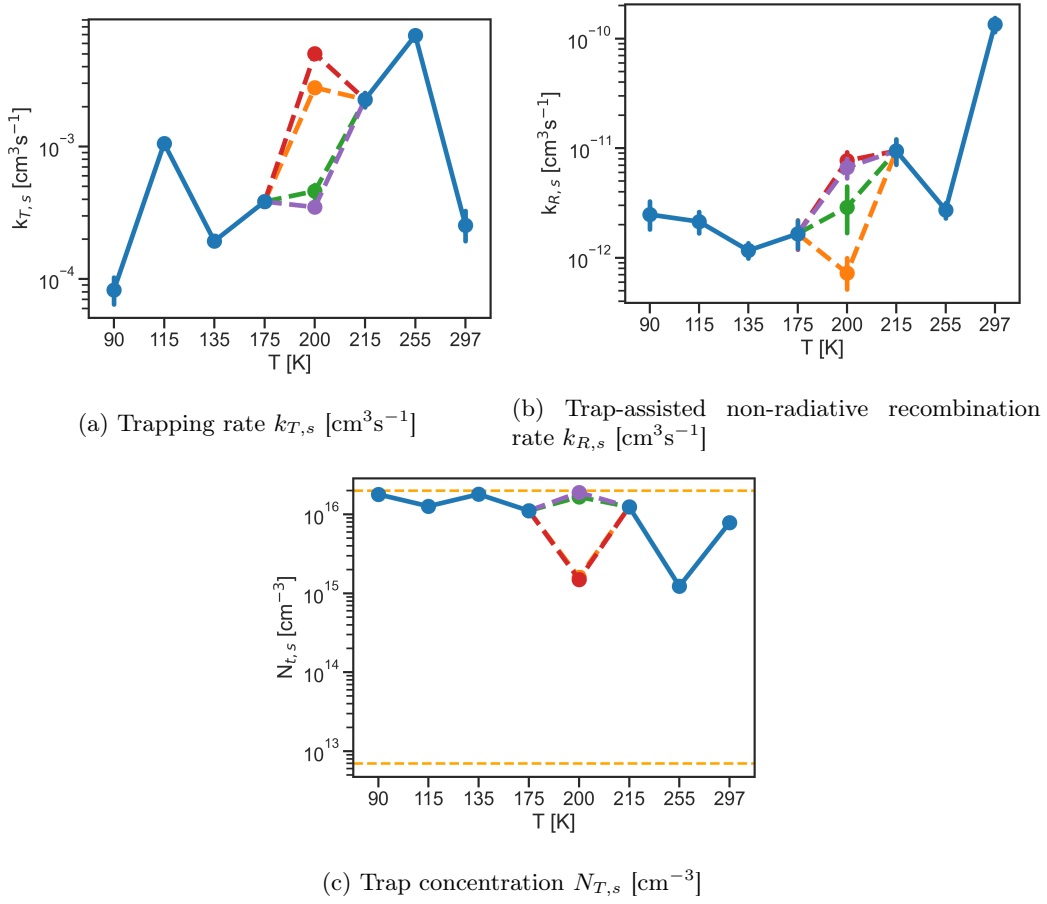


Figure 44: Shallow trap fit parameter values plotted for varying temperatures.

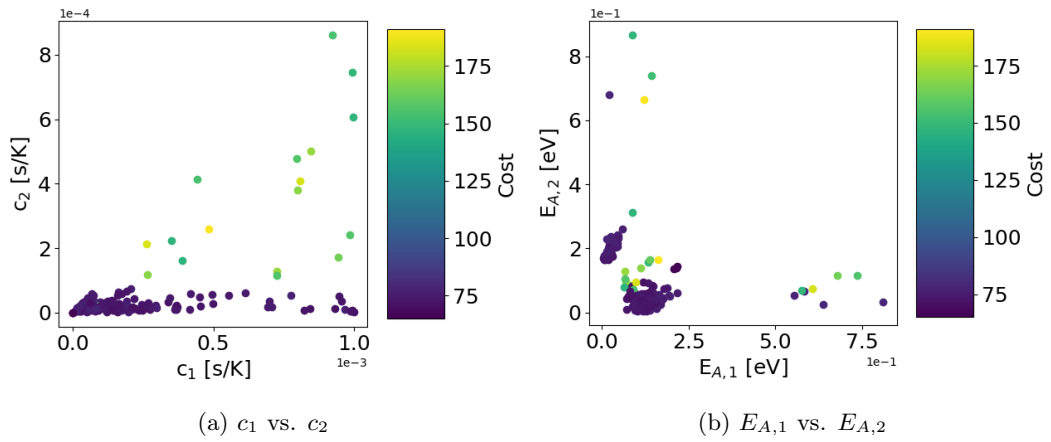


Figure 45: Scatter plots of the full set of repetitions for the extracted parameter values of both exponentials in pixel D2P1.

	<b>D1</b>	<b>P1</b>	<b>D1</b>	<b>P2</b>
<b>Best fit</b>	<i>DLTS</i>	<i>TID</i>	<i>DLTS</i>	<i>TID</i>
$c_1$ ( $10^{-4} T^{-1}$ )	$1.34 \cdot 10^{-4}$	$1.13 \cdot 10^{-4}$	$1.54 \cdot 10^{-5}$	$4.63 \cdot 10^{-1}$
$E_{A,1}$ ( $10^{-1}$ eV)	2.8	$6.33 \cdot 10^{-1}$	2.63	$8.64 \cdot 10^{-1}$
$c_2$ ( $10^{-4} T^{-1}$ )	$2.29 \cdot 10^{-5}$	$1.66 \cdot 10^{-2}$	$1.53 \cdot 10^{-5}$	$2.72 \cdot 10^{-2}$
$E_{A,2}$ ( $10^{-1}$ eV)	2.48	1.06	3.36	$9.74 \cdot 10^{-1}$
<b>Top 15%</b>	<i>DLTS</i>	<i>TID</i>	<i>DLTS</i>	<i>TID</i>
$c_1$ ( $10^{-4} T^{-1}$ )	$1.06 \pm 1.19$	$1.39 \pm 1.05$	$1.60 \pm 2.42$	$1.38 \pm 1.66$
$E_{A,1}$ ( $10^{-1}$ eV)	$1.37 \pm 0.553$	$0.766 \pm 0.154$	$1.36 \pm 0.385$	$0.664 \pm 0.127$
$c_2$ ( $10^{-4} T^{-1}$ )	$(7.89 \pm 9.65) \cdot 10^{-2}$	$(9.97 \pm 9.01) \cdot 10^{-2}$	$(4.33 \pm 5.24) \cdot 10^{-2}$	$(5.33 \pm 2.41) \cdot 10^{-2}$
$E_{A,2}$ ( $10^{-1}$ eV)	$9.30 \cdot 10^{-2} \pm 5.09 \cdot 10^{-2}$	$0.776 \pm 0.202$	$1.07 \pm 5.13 \cdot 10^{-2}$	$0.109 \pm 0.247$
<b>All</b>	<i>DLTS</i>	<i>TID</i>	<i>DLTS</i>	<i>TID</i>
$c_1$ ( $10^{-4} T^{-1}$ )	$1.51 \pm 2.26$	$1.89 \pm 1.37$	$1.45 \pm 2.41$	$2.08 \pm 1.54$
$E_{A,1}$ ( $10^{-1}$ eV)	$1.37 \pm 1.27$	$2.44 \pm 2.41$	$1.62 \pm 1.51$	$2.08 \pm 2.34$
$c_2$ ( $10^{-4} T^{-1}$ )	$0.389 \pm 1.09$	$0.547 \pm 0.694$	$0.427 \pm 1.24$	$0.604 \pm 0.796$
$E_{A,2}$ ( $10^{-1}$ eV)	$1.15 \pm 1.13$	$1.48 \pm 1.86$	$1.32 \pm 1.32$	$1.18 \pm 1.60$

	<b>D2</b>	<b>P1</b>	<b>D2</b>	<b>P2</b>
<b>Best fit</b>	<i>DLTS</i>	<i>TID</i>	<i>DLTS</i>	<i>TID</i>
$c_1$ ( $10^{-4} T^{-1}$ )	$1.08 \cdot 10^{-3}$	$3.02 \cdot 10^{-1}$	$5.56 \cdot 10^{-3}$	$4.13 \cdot 10^{-2}$
$E_{A,1}$ ( $10^{-1}$ eV)	2.18	$3.04 \cdot 10^{-1}$	1.62	1.75
$c_2$ ( $10^{-4} T^{-1}$ )	$1.06 \cdot 10^{-3}$	$1.46 \cdot 10^{-2}$	$3.05 \cdot 10^{-6}$	$3.70 \cdot 10^{-3}$
$E_{A,2}$ ( $10^{-1}$ eV)	1.43	1.73	2.85	1.5
<b>Top 15%</b>	<i>DLTS</i>	<i>TID</i>	<i>DLTS</i>	<i>TID</i>
$c_1$ ( $10^{-4} T^{-1}$ )	$2.16 \pm 2.47$	$1.51 \pm 1.37$	$(4.34 \pm 3.68) \cdot 10^{-3}$	$1.23 \pm 0.836$
$E_{A,1}$ ( $10^{-1}$ eV)	$1.13 \pm 0.446$	$0.493 \pm 0.272$	$1.93 \pm 0.449$	$1.08 \pm 0.228$
$c_2$ ( $10^{-4} T^{-1}$ )	$0.208 \pm 0.152$	$0.749 \pm 0.501$	$(9.22 \pm 6.47) \cdot 10^{-6}$	$(4.27 \pm 3.15) \cdot 10^{-2}$
$E_{A,2}$ ( $10^{-1}$ eV)	$0.604 \pm 0.541$	$0.516 \pm 0.668$	$2.91 \pm 0.162$	$1.01 \pm 0.208$
<b>All</b>	<i>DLTS</i>	<i>TID</i>	<i>DLTS</i>	<i>TID</i>
$c_1$ ( $10^{-4} T^{-1}$ )	$2.29 \pm 2.73$	$2.24 \pm 2.24$	$1.63 \pm 2.90$	$1.45 \pm 1.76$
$E_{A,1}$ ( $10^{-1}$ eV)	$1.30 \pm 1.18$	$2.07 \pm 2.51$	$2.97 \pm 2.37$	$2.16 \pm 2.18$
$c_2$ ( $10^{-4} T^{-1}$ )	$0.495 \pm 1.14$	$0.748 \pm 0.653$	$0.466 \pm 1.53$	$0.304 \pm 0.521$
$E_{A,2}$ ( $10^{-1}$ eV)	$0.900 \pm 1.15$	$1.42 \pm 1.76$	$1.46 \pm 1.40$	$1.48 \pm 1.70$

Table 3: Extracted fitting parameters of capacitance transients. DTLS values are measured using a 10 ms filling pulse, while the TID traces are measured using a 1 second pulse. For these measurements, two pixels from two different devices are used.